Volume 12
Number 7
21 February 2024
Pages 1669–1938

Journal of Materials Chemistry B

Materials for biology and medicine

rsc.li/materials-b

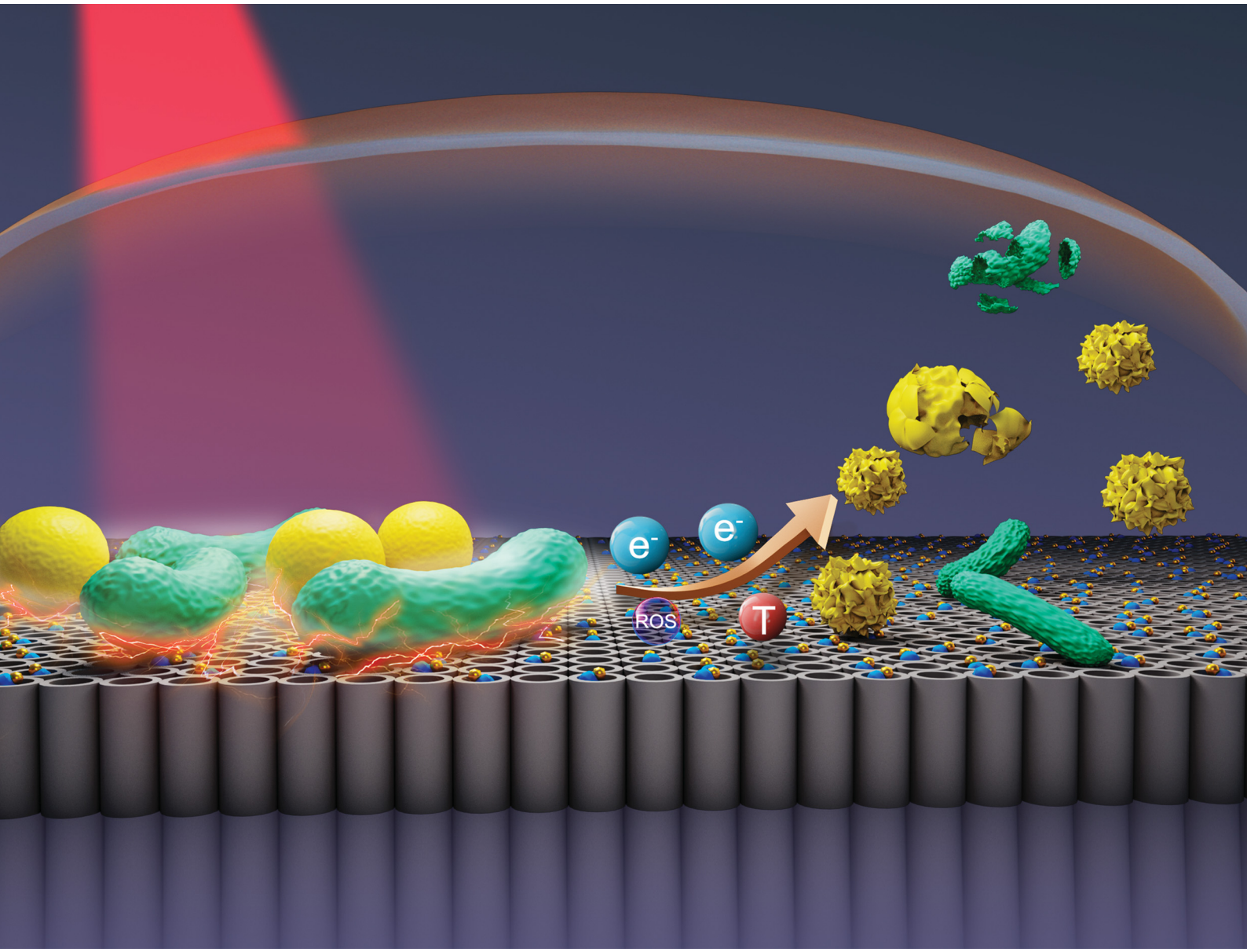

ISSN 2050-750X

ROYAL SOCIETY OF CHEMISTRY

PAPER

Lin Xiang, Xuemei Zhou *et al.*

Regulation of the upconversion effect to promote the removal of biofilms on a titanium surface *via* photoelectrons

Journal of Materials Chemistry B

ROYAL SOCIETY OF CHEMISTRY

PAPER

View Article Online
View Journal | View Issue

Cite this: J. Mater. Chem. B, 2024, 12, 1798

Regulation of the upconversion effect to promote the removal of biofilms on a titanium surface *via* photoelectrons†

Kai Wang,[a] Yufei Tang,[b] Keyi Yao,[a] Shuqi Feng,[b] Bingfeng Wu,[b] Lin Xiang *[b] and Xuemei Zhou *[a]

Received 27th October 2023,
Accepted 31st December 2023

DOI: 10.1039/d3tb02542j

rsc.li/materials-b

Biofilms on public devices and medical instruments are harmful. Hence, it is of great importance to fabricate antibacterial surfaces. In this work, we target the preparation of an antibacterial surface excited by near-infrared light *via* the coating of rare earth nanoparticles (RE NPs) on a titanium surface. The upconverted luminescence is absorbed by gold nanoparticles (Au NPs, absorber) to produce hot electrons and reactive oxygen species to eliminate the biofilms. The key parameters in tuning the upconversion effect to eliminate the biofilms are systematically investigated, which include the ratios of the sensitizer, activator, and matrix in the RE NPs, or the absorber Au NPs. The regulated RE NPs exhibit an upconversion quantum yield of 3.5%. Under illumination, photogenerated electrons flow through the surface to bacteria, such as *E. coli*, which disrupt the breath chain and eventually lead to the death of bacteria. The mild increase of the local temperature has an impact on the elimination of biofilms on the surface to a certain degree as well. Such a configuration on the surface of titanium exhibits a high reproducibility on the removal of biofilms and is functional after the penetration of light using soft tissue. This work thus provides a novel direction in the application of upconversion materials to be used in the fabrication of antibacterial surfaces.

1. Introduction

Titanium (Ti) and titanium alloys have been widely used in industry, such as aerospace, engineering, marine, and biomedicines, due to their low density, high hardness, and exceptional corrosion and heat resistance.[1–3] However, the surface of titanium or its alloys is prone to bacterial, viral and microbial adhesion. This may hinder its applications, in particular in biomedicines, that require high repellency of microbial contamination (*e.g.*, bacterial adhesion or biofilm formation).[4] One possible solution to avoid microbial contamination or eliminate biofilm growth is to fabricate an antibacterial surface, which can be ideally activated by external energy using portable devices, such as near-infrared (NIR) light, or sonication.

NIR light has a biological window of 700–1100 nm, which can penetrate several millimeters in soft tissues, and is nontoxic for organisms.[5,6] The applications of NIR light provide the potentials for the implants to be used in the host body, and the low excitation energy of NIR light may be substituted by other external sources. Therefore, the NIR light-induced photodynamic and photothermal effect are frequently employed to eliminate biofilms or kill cancer cells. Photodynamic therapy takes the advantage of the reactive oxygen species (ROS) produced on active surfaces to damage bacterial cell membranes, inactivate DNA and proteins, or to cause oxidative stress in bacteria.[7,8] However, to generate ROS (OH radicals or singlet oxygen species), certain requirements on the energy of incident light need to be met;[8] that is, the energy of incident light should be sufficient to excite the materials. Moreover, the energetic positions of a semiconductive material or polymer should meet the redox potential of ROS, or the incident photon frequency needs to match the localized surface plasmon resonance (LSPR) effect of noble metals. Furthermore, a high concentration of ROS may damage normal biological tissues.[9] Therefore, the dose of applied ROS needs to be considered. Thus far, the dosage has not been well controlled or systematically investigated.[10,11] For photothermal therapy, the target temperatures in several systems are higher than the values that the cells can stand. Therefore, it is important to be extremely careful with the operation during treatment.[12–14]

[a] School of Chemical Engineering, Sichuan University, Chengdu 610065, China. E-mail: xuemeizhou@scu.edu.cn
[b] State Key Laboratory of Oral Diseases & National Center for Stomatology & National Clinical Research Center for Oral Diseases, West China Hospital of Stomatology, Sichuan University, Chengdu 610041, Sichuan, China. E-mail: dentistxiang@126.com

† Electronic supplementary information (ESI) available. See DOI: https://doi.org/10.1039/d3tb02542j

During irradiation, NIR light can also produce electrons in addition to a thermal effect or ROS. However, in most of the reported studies, the impact of the electron on the behaviors of the materials is overlooked. This may be because low-energy NIR light (compared to ultraviolet light (UV) and Visible light) can only generate low-energy electrons. Recent studies have demonstrated that an extracellular electron transfer (EET) can target aerobic bacteria, such as *Staphylococcus aureus* (*S. aureus*) and *Escherichia coli* (*E. coli*).[15,16] Therefore, the current flow between the aerobic bacteria and the surface of titanium can lead to bacterial death.

Rare earth (RE) element materials, which can be excited by NIR light and upconvert partial incident energy to the visible region or UV region, have been employed as an antenna and improved the energy of NIR-generated active species.[17] Upconversion is a nonlinear optical process in which two or more photons are absorbed consecutively, resulting in the wavelength of emission light being shorter than that of the excitation wavelength (anti-Stokes emission).[17,18] For example, a core–shell material with β-$NaYF_4$: Yb^{3+}, Tm^{3+} as the core and TiO_2 as the shell can convert NIR light from 980 nm to UV light, improving the photocatalytic performance of TiO_2. Besides, an absorber is needed to absorb the light emitted by the RE materials. Noble metals, such as Au and Ag, can absorb light in the visible region due to the plasmonic effect, and can enhance the local electric field near RE materials or at the interface between RE materials and noble metals to amplify the upconversion luminescence of RE materials.[19,20]

Moreover, the sensitizer and activator also have great influence on the upconversion luminescence efficiency. In general, the sensitizer and activator need to be regulated at an appropriate concentration to avoid energy dissipation, known as concentration quenching, and ensure high upconversion luminescence intensity. Overdosing of the sensitizer or activator may lead to the decrease of the excited state and the attenuation of the upconversion emission, which may be ascribed to the long distance energy migration or surface defects of the dominant sensitizer, local cross relaxation or phonon assistance of the dominant activator.[21,22] Therefore, it is essential to regulate the composition of RE NPs and couple with absorbers to enhance the luminescence process.

In this work, we target the employment of photoelectrons on the surface of titanium for efficient biofilm removal by regulating the upconversion of RE NPs on TiO_2. The titanium dioxide (TiO_2) nanotube arrays are grown on a Ti substrate, loaded with RE NPs, and modified with gold nanoparticles (Au NPs). Anodization of the Ti substrate was applied due to the high control on the morphology, good adhesion of the oxide layer on the substrate, and surface porous structure with excellent cell colonization potential. Au NPs are selected due to the high biocompatibility. For the RE NPs, $NaYF_4$ is chosen as a matrix due to the low phonon energy, Yb^{3+} is used as sensitizer based on the absorption capacity of NIR at 980 nm, and Er^{3+} is doped as activator to tune the emission wavelength of the upconversion luminescence (visible region).

2. Experimental section

2.1. Preparation of Au_α–$RE_\beta(Yb_\gamma$–$Er_\delta)/TiO_2$

TiO_2 nanotube arrays were prepared by anodization on titanium foils (0.1 mm thickness, purity 99.6%+). First, the titanium foils were cleaned in acetone, ethanol, and deionized water separately by sonication, and dried in a nitrogen stream. Then, TiO_2 nanotube arrays were grown by anodization in an ethylene glycol electrolyte consisting of 0.2 M NH_4F (General-reagent, ≥98.0%) and 1 M H_2O for 20 min at 60 V using a power supply (Yangzhou YuMing DC POWER Supply Co., Ltd, YM-K 100V 20A) in a two-electrode configuration with a platinum counter electrode. After anodization, the sample was cleaned with ethanol and dried in a nitrogen stream.

Au was decorated on TiO_2 nanotube arrays using a sputter device (SBC-12) at a current of 8 mA for 1 min and 3 min, respectively. Then, the Au/TiO_2 sample was annealed in a muffle furnace (PI-KEM Ltd, KSL-1200X) at 450 °C for 1 h to convert the amorphous tube layers to a crystal structure.

Rare earth compounds were deposited onto the Au/TiO_2 layer using a deposition–precipitation method. For Au_1–$RE_1(Yb_{20}$–$Er_2)/TiO_2$, 0.25 g urea (Damas-beta, 99%+) was dissolved in 25 mL deionized water, then 250 μL $Y(NO_3)_3$ (Damas-beta, 99.99%) at a concentration of 1.0 M, 100 μL $Yb(NO_3)_3$ (Guobiao (Beijing) Testing & Certification Co., Ltd, 1000 μg mL^{-1}) at a concentration of 0.63 M, and 15 μL $Er(NO_3)_3$ (Alfa Aesar, 99.9%) at a concentration of 0.4 M were added into the above solution in turn. The solution was then placed in a water bath at 90 °C for 1 h. Then, the as-prepared Au–RE/TiO_2 thin layer was washed several times using deionized water and dried in a nitrogen stream. Finally, the samples were sealed in a Teflon-lined stainless autoclave with 200 μL precursor solution and treated at 100 °C for 30 min, and then washed with deionized water and dried in a nitrogen stream. The precursor solution consisted of 3 mL 0.1 M HF, 0.1 g NaF, and 8 mL deionized water. Additionally, samples with a RE deposition time of 0 and 3 h, Yb^{3+} and Er^{3+} concentrations of 0, 203 μL $Yb(NO_3)_3$ solution and 0, 32 μL $Er(NO_3)_3$ solution were prepared. Samples were named according to different Au sputtering time, RE deposition time, and concentration of Yb^{3+} and Er^{3+}. The composition of all samples decorated with Au NPs and RE NPs can be found in Table S1 (ESI†).

2.2. Characterization on the thin film

The scanning electron microscope (SEM) images of the samples were recorded using JSM-7610F (JEOL Ltd, Japan). X-ray diffraction (XRD) patterns were collected using an X'pert Philips PMD diffractometer with a Panalytical X'celerator detector, using graphite-monochromatized Cu Kα radiation (λ = 1.54056 Å). X-ray photoelectron spectroscopy (XPS, AXIS Ultra DLD, Kratos, Japan) was used for chemical compositional analysis of the samples. XPS spectra were acquired using monochromatic X-rays with a pass energy of 23.5 eV. The survey spectrum was performed at an accelerated voltage of 10 kV and 7 mA, and the high-resolution spectrum for each element was carried out at an accelerated voltage of 10 kV and 15 mA. All of the XPS

element peaks were shifted to the C 1s standard position (284.8 eV). The power density of the 980 nm NIR laser was measured with an optical power densitometer (Zhongjiaojinyuan Instruments). The UV-vis absorbance spectra measurements were conducted on a UV-vis spectroscope (Agilent Cary 60, America).

2.3. Photoelectrochemical characterization

Photoelectrochemical characterization was carried out with an electrochemical setup consisting of a three-electrode configuration, with an Ag/AgCl reference electrode and a Pt plate as a counter electrode. Photocurrent spectra were acquired in 0.1 M (Na_2SO_4) at a potential of 500 mV (Ag/AgCl) with a 980 nm NIR (669 mW cm^{-2}) laser as the irradiation source. The photocurrent was recorded for 30 s in cycles.

2.4. Photothermal ability evaluation

The photothermal conversion performance of the samples was measured by a photothermal instrument (Flir Systems, E6390). All samples were continuously irradiated for 15 min in a 24-well plate with 500 μL phosphate buffer saline (PBS) solution using a 980 nm NIR laser (669 mW cm^{-2}). The temperature of the samples was recorded every 30 s and thermal images were taken after 15 min of illumination. Additionally, to demonstrate the photothermal stability of Au_1–$RE_1(Yb_{20}$–$Er_2)/TiO_2$, a cyclic heating and cooling experiment was performed with a cycle of continuous irradiation for 15 min and darkness for 15 min. The heating and cooling process was repeated for 3 cycles, and the temperature was recorded every 1 min.

2.5. ROS generation capacity assays

The photocatalytic activity was evaluated by detecting the ROS generation capacity under 980 nm NIR irradiation (669 mW cm^{-2}). The ROS could be captured by an aqueous solution of rhodamine B (RhB). The different samples were incubated with 3 mL of RhB (8 mg L^{-1}) under dark condition for 10 min to achieve adsorption/desorption equilibrium. Then, samples were treated with the 980 nm NIR laser for 30 min, and the absorbance of the supernatant was measured using an UV-vis spectroscope every 10 min. 0.8 mM Fe^{2+} and 0.8 mM H_2O_2 were added to release ROS and the absorbance of the RhB solution was measured every 30 s.

Additionally, 9,10-anthracenediylbis(methylene) dimalonic acid (ABDA), methyl violet (MV), and nitro blue tetrazolium (NBT) were employed to determine the amounts of $^1O_2$, ·OH, and $\cdot O_2^-$, produced by Au_1–$RE_1(Yb_{20}$–$Er_2)/TiO_2$ under NIR illumination. Samples were immersed into 3 mL of ABDA (50 μM), MV (15 mg L^{-1}), or NBT (0.2 mM) under dark conditions for 10 min to achieve adsorption/desorption equilibrium, and then irradiated with a 980 nm NIR laser for 60 min. The absorbance spectra were acquired by the UV-vis spectroscope every 15 min.

2.6. Antibacterial activity test

Staphylococcus aureus (*S. aureus*, ATCC 43300) and *Escherichia coli* (*E. coli*, BNCC 269342) were used to evaluate the antibacterial property of different samples. First, samples (0.5 cm × 0.5 cm) were placed in a 24-well plate with 500 μL diluted bacterial solution (~10^7 CFU mL^{-1}) cultured Luria-Bertain (LB) broth, and cultured at 37 °C for 24 h to form the bacterial biofilm. Then, samples were placed face-on in a 24-well plate with 500 μL PBS, and were irradiated continuously with or without the 980 nm NIR laser (669 mW cm^{-2}) for 15 min. After irradiation, samples were washed with 1 mL PBS for three times, and transferred to a clean 24-well plates with 500 μL PBS. Then, the samples were treated using ultrasound and the obtained suspensions were diluted. A 10-μL volume of diluted bacterial suspension was then collected and spread onto the LB agar plate, and cultured at 37 °C for 24 h. Finally, the bacterial colonies on the plates were photographed, and the corresponding antibacterial efficiency was calculated, as follows:

$$\text{Antibacterial efficiency}(\%) = \frac{\text{CFU}_{\text{Ctrl}} - \text{CFU}_{\text{Experiment}}}{\text{CFU}_{\text{Ctrl}}} \times 100$$

2.7. Evaluation of the activity of respiratory chain dehydrogenase

The activity of respiratory chain dehydrogenase was evaluated using iodonitrotetrazolium chloride (INT). Firstly, samples (0.8 cm × 0.8 cm) were incubated with 500 μL *E. coli* solution (~10^7 CFU mL^{-1}) in a 24-well plate at 37 °C for 24 h. Then, bacteria on the back of samples were killed by alcohol. The samples were washed with PBS and put into another 24-well plate with 500 μL PBS. For the irradiation groups, samples were constantly irradiated for 15 min using a 980 nm NIR laser (669 mW cm^{-2}). Next, samples were transferred to another 24-well plate with 500 μL PBS and treated with ultrasound. The obtained solution after ultrasound was mixed with 500 μL INT solution (0.5 wt%) and stirred for 1 h. The bacterial solution without the sample and NIR-treatment was used as the controls. Then, 450 μL formaldehyde was added into the solution and stirred for 10 min. The solution was centrifuged under 9000 rpm, and the obtained precipitates were stirred in a 3 mL acetone/ethanol solution (1 : 1) for 30 min. Finally, the OD value of the supernatant at 490 nm was detected by UV-vis spectroscope.

2.8. Detection of the extracellular current in bacteria

The EET mechanism of Au_1–$RE_1(Yb_{20}$–$Er_2)/TiO_2$ was verified by detecting the current–potential (*I*–*V*) curves. The TiO_2 groups were used as the controls. The *I*–*V* curves were tested using a three-electrode device with a Pt plate as a counter electrode and a calomel electrode (SCE) as a reference electrode. 5 mM $K_3[Fe(CN)_6]$ was used as an electrolyte. For Au_1–$RE_1(Yb_{20}$–$Er_2)/TiO_2$ and TiO_2 with living *E. coli* on the surface, samples were inoculated with *E. coli* (~10^7 CFU mL^{-1}) and cultured at 37 °C for 30 min, and then were washed 3 times with PBS. For samples with dead *E. coli* on the surface, the bacteria were fixed with 2.5% glutaraldehyde fixative after inoculation and gradient dehydration with ethanol

(30%, 50%, 85%, 100%), and then the samples were washed with PBS. Next, the *I–V* curves were tested on the electrochemical workstation with the working electrode potential between 0 mV and 500 mV, under 980 nm NIR laser irradiation or dark condition.

2.9. Measurement of the absolute quantum yield of RE NPs

The upconversion quantum yield (QY) of the RE element was used to describe the upconversion efficiency. This test was performed using a FLS1000 Fluorescence Spectrofluorometer at room temperature. Samples were excited using a 980 nm laser (2 W cm^{-2}), and the emission spectra and excitation spectra of the samples and blank were recorded. The QY was calculated, as follows:

$$\mathrm{QY}(\%) = \frac{I_{\mathrm{em,sample}} - I_{\mathrm{em,blank}}}{I_{\mathrm{ex,blank}} - I_{\mathrm{ex,sample}}} \times 100\%$$

where $I_{\mathrm{em,sample}}$ and $I_{\mathrm{em,blank}}$ were the integrated intensity of the emission spectrum for the sample and blank, respectively. $I_{\mathrm{ex,sample}}$ and $I_{\mathrm{ex,blank}}$ were the integrated intensity of the excitation spectrum for the sample and blank, respectively.

2.10. CCK-8 assays

The CCK-8 assays were designed to evaluate the proliferation activity of the MC3T3-E1 cells on different surfaces. Each sample (4 mm × 4 mm) was seeded with 1×10^4 MC3T3-E1 cells, and cultured for 1, 3, and 5 days. Then, 100 μL of mixed liquid (90 μL fresh culture medium and 10 μL CCK-8 solution) was added to each harvested sample. After being incubated under dark conditions for 1 hour at 37 °C, the solution was collected. The absorbance value was measured at a wavelength of 450 nm. For CCK-8 assays with NIR illumination, on day 1, the samples were irradiated with 980 nm NIR for 15 min and washed with PBS before adding the mixed liquid (90 μL fresh culture medium and 10 μL CCK-8 solution). The cell proliferation rate was calculated according to the following formula.

$$\text{Cell proliferation}(\%) = \frac{\mathrm{OD_{Experiment}}}{\mathrm{OD_{Ctrl}}} \times 100$$

2.11. The release of metal ions from the surface

The release of metal ions (Au, Y, Yb, Er) from the sample surface in a simulated body fluid (SBF) was detected. Specifically, the Au_1–$RE_1(Yb_{20}$–$Er_2)/TiO_2$ sample (0.5 cm × 0.5 cm) was put into a vial containing 10 mL SBF and placed at 37 °C and the solution was sampled at days 1, 3, 7, and 14. The concentration of metal ions in the solutions were detected by ICP-OES (Agilent 5100 SVDV, America) with a detection limit of 1 ppb. Due to the low concentration of ions, each sample solution was measured three times and an error bar was provided.

3. Results and discussions

3.1. Synthesis

The TiO_2 nanotube arrays are grown tightly on a Ti metal substrate by self-organized anodization (Scheme 1), and the Au NPs and RE NPs (Y-, Yb- and Er-) are decorated in sequence. In brief, the TiO_2 nanotube arrays are prepared by anodizing a Ti metal in a NH_4F/ethylene glycol electrolyte at 60 V for 20 min to reach a thickness of ~7.5 μm (Fig. S1, ESI†). The Au NPs are decorated by physical vapor sputtering deposition, and the size/amount of Au NPs is regulated by sputtering time (Table S1, ESI†). The Au/TiO_2 NTAs is annealed at 450 °C in air to prepare the Au nanoparticles. Afterwards, the RE NPs are precipitated on the surface by coprecipitation.[23] The amount of RE NPs is regulated by deposition time. The ratio and amount of RE precursors are investigated to tune the luminescence effect of RE NPs (details are given in Table S1, ESI†). The matrix material of the RE NPs is converted to $NaYF_4$ after treatment in NaF solution. The as-prepared samples are annotated as Au_α–$RE_\beta(Yb_\gamma$–$Er_\delta)/TiO_2$ (Table S1, ESI†). In the case of zero for a given component, the annotation is omitted.

3.2. Photoelectrochemical performance

The density of the photoelectron plays a key role in assessing the ability to remove biofilms. Therefore, the transient photocurrent density in cycles was recorded under NIR (Fig. 1). The impact of the absorber, Au NPs, on the photocurrent density is shown in Fig. 1a. $RE_1(Yb_{20}$–$Er_2)/TiO_2$ generates a

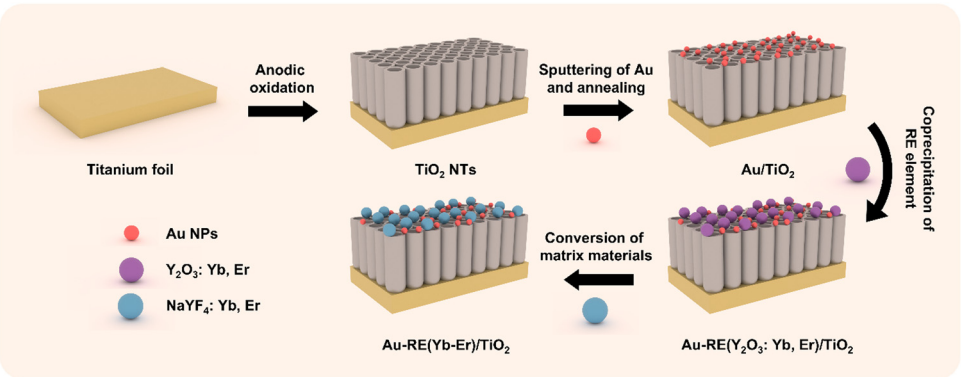

Scheme 1 Schematic drawing of the synthetic process of Au–RE(Yb–Er)/TiO_2.

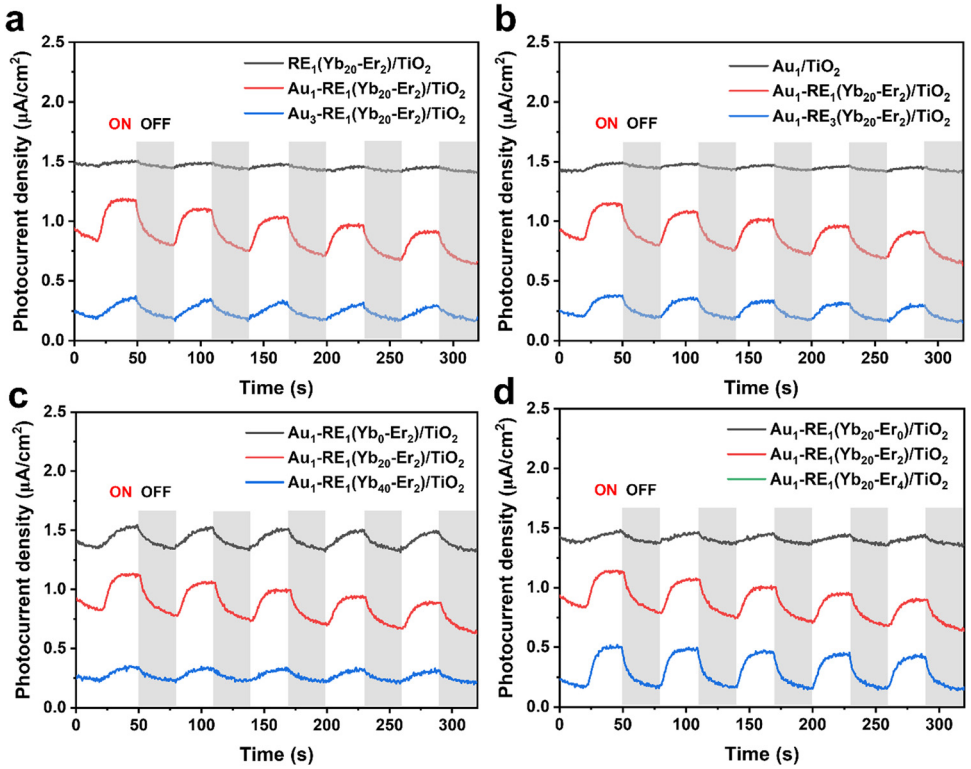

Fig. 1 Photocurrent responses of different samples under the irradiation of NIR in the variation of (a) Au loading, (b) RE deposition amount, (c) concentration of Yb^{3+}, and (d) concentration of Er^{3+}.

low photocurrent density (0.06 μA cm^{-2}) due to the absence of Au NPs, indicating that the mismatch of the energetic positions between the luminescence of NPs and TiO_2 leads to low photoelectron conversion efficiency. In the presence of Au NPs, the photocurrent density of Au_1–$RE_1(Yb_{20}$–$Er_2)/TiO_2$ significantly increases to 0.38 μA cm^{-2}, but decreases to 0.21 μA cm^{-2} for Au_3–$RE_1(Yb_{20}$–$Er_2)/TiO_2$, suggesting that too high amount of Au is not beneficial for luminescence light absorption or conversion.

The investigation on the amount of matrix $NaYF_4$, in terms of the total RE NPs (by RE deposition time), is shown in Fig. 1b. Without RE NPs, Au_1/TiO_2 produces the lowest photocurrent density (0.05 μA cm^{-2}). At too high amount of RE NPs, that is, the deposition time of RE NPs is 3 hours, the photocurrent density of Au_1–$RE_3(Yb_{20}$–$Er_2)/TiO_2$ is 0.18 μA cm^{-2}, which is lower than that of Au_1–$RE_1(Yb_{20}$–$Er_2)/TiO_2$ (0.38 μA cm^{-2}).

The concentration of sensitizer and activator affects the absorption and conversion of 980 nm NIR by RE NPs, respectively. Fig. 1c and d show the impact of the sensitizer and activator in the variation of the concentration of Yb^{3+} and Er^{3+} in the RE NPs. In the absence of the Yb^{3+} concentration (0%) or with a higher Yb^{3+} concentration (40%), a lower photocurrent density is obtained, that is 0.18 μA cm^{-2} for Au_1–$RE_1(Yb_0$–$Er_2)/TiO_2$, and 0.13 μA cm^{-2} for Au_1–$RE_1(Yb_{40}$–$Er_2)/TiO_2$ (Fig. 1c), which may be ascribed to the energy dissipation. The results thus suggest that 20 wt% Yb^{3+} is suitable as an activator for the $NaYF_4$ matrix to convert 980 nm NIR.

For the Er^{3+} concentration (Fig. 1d), in the absence of Er^{3+} (0 wt%), the photocurrent density is 0.1 μA cm^{-2} for Au_1–$RE_1(Yb_{20}$–$Er_1)/TiO_2$, which is lower than that for Au_1–$RE_1(Yb_{20}$–$Er_2)/TiO_2$. At higher concentration (4 wt%), the photocurrent density for Au_1–$RE_1(Yb_{20}$–$Er_4)/TiO_2$ (0.33 μA cm^{-2}) is similar to that of Au_1–$RE_1(Yb_{20}$–$Er_2)/TiO_2$, suggesting that 2 wt% of Er in RE NPs is sufficient to activate the luminescence.

The results in Fig. 1 thus demonstrate that Au_1–RE_1-$(Yb_{20}$–$Er_2)/TiO_2$ with a RE deposition time of 1 h, 20 wt% Yb, and 2 wt% Er, and 1 min of Au sputtering time, can generate high photocurrent under the 980 nm NIR irradiation, indicating the sample has excellent absorption and conversion of 980 nm light. The absorbed NIR by RE NPs emits in the visible region, which can excite the Au NPs and generate hot electrons on the TiO_2 nanotube arrays.

3.3. Morphology and composition analysis impact on the photoelectron conversion efficiency

The scanning electron microscope (SEM) images of TiO_2 show that the top diameter of the tubes is an average of 54 ± 5 nm (Fig. 2a). When the Au sputtering time is 1 min, the Au NPs are uniformly distributed on the surface of the substrate with uniform size (Fig. 2b). However, as the Au sputtering time increased to 3 min, larger size distributions of the Au NPs are observed, which may impact the absorption of Au NPs (Fig. S2, ESI†). After decorating with RE NPs, Au_1–$RE_1(Yb_{20}$–$Er_2)/TiO_2$ exhibits a relatively homogenous surface with a small change

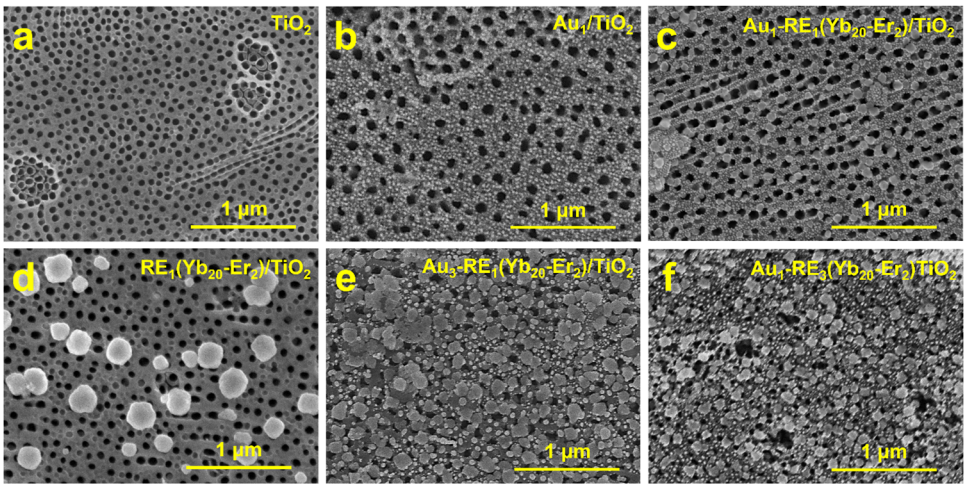

Fig. 2 SEM images of different samples. (a) TiO_2, (b) Au_1/TiO_2, (c) $Au_1–RE_1(Yb_{20}–Er_2)/TiO_2$, (d) $RE_1(Yb_{20}–Er_2)/TiO_2$, (e) $Au_3–RE_1(Yb_{20}–Er_2)/TiO_2$, and (f) $Au_1–RE_3(Yb_{20}–Er_2)/TiO_2$.

on the top diameter of TiO_2 under SEM (Fig. 2c), showing an average diameter of Au NPs of 20 ± 3 nm and RE NPs of 64 ± 9 nm (Fig. S3, ESI†). The results thus suggest that the decoration of RE NPs and the following treatment do not change the morphology of the Au NPs significantly.

Fig. 2d shows $RE_1(Yb_{20}–Er_2)/TiO_2$ without Au NPs. For $Au_3–RE_1(Yb_{20}–Er_2)/TiO_2$, the size of Au NPs is 55 ± 16 nm, indicating that the size of the Au NPs increases with the extension of the Au sputtering time (Fig. 2e). During the annealing treatment, the Au NPs were formed, and the patterned support had an impact on the morphology of the NPs.[24] Moreover, with the increase of the amount of RE NPs, in terms of the deposition time (Fig. 2f), a significantly higher coverage of RE NPs is observed. Noticeably, for $Au_1–RE_3(Yb_{20}–Er_2)/TiO_2$, most of the top mouth of the TiO_2 NTAs is covered, and the diameter of the top mouth decreases.

The energy dispersive X-ray spectroscopy (EDS) mapping of $Au_1–RE_1(Yb_{20}–Er_2)/TiO_2$ in Fig. 2c shows the uniform distribution of Ti, O, F, Au, Y, Yb, and Na (Fig. S4, ESI†), demonstrating a uniform distribution of RE NPs on TiO_2. No plausible intensity for Er in EDS is shown, which may be due to the low concentration on the surface.

In addition to EDS, X-ray photoelectron spectra (XPS) were acquired to investigate the surface composition and chemical state of elements. The peaks of C 1s, Ti 2p, O 1s, Au 4f, Y 3d, Yb 4d, Na 1s, and F 1s are marked in the survey spectra of all samples, and the atomic percentage of each element is calculated based on the high-resolution spectra (Fig. 3a and Fig. S5, Table S2, ESI†). No other elements from contamination are detected in XPS. Clearly, with the increase of Au loading, the atomic ratio of Au increases from 6.3 for $Au_1–RE_1(Yb_{20}–Er_2)/TiO_2$ to 12.4 for $Au_3–RE_1(Yb_{20}–Er_2)/TiO_2$. When the atomic ratio is normalized to Ti, the atomic ratio of Au of $Au_1–RE_1(Yb_{20}–Er_2)/TiO_2$ is 1.47, which is smaller than that of $Au_3–RE_1(Yb_{20}–Er_2)/TiO_2$ (1.97), indicating that the Au content of the samples increases with the increase of the Au sputtering time. With the increase of the RE deposition amount, the atomic concentration of Y increases from 4.1 for $Au_1–RE_1(Yb_{20}–Er_2)/TiO_2$ to 7.4 for $Au_1–RE_3(Yb_{20}–Er_2)/TiO_2$, indicating a higher density of RE NPs on the surface. The atomic ratio between Na, Y and F is close to 1 : 1 : 4, suggesting that the existing elements are in the $NaYF_4$ composition.

The high-resolution spectrum for Ti 2p (Fig. 3b) shows double peaks of Ti $2p_{3/2}$ and Ti $2p_{1/2}$ of different samples with an energy split of 5.8 eV. The binding energy locations of Ti 2p are found to be consistent with the Ti^{4+} chemical state in TiO_2, suggesting that the support is TiO_2 in the as-prepared samples. The Au 4f spectra of samples with different Au loading shows that Au 4f of $Au_1–RE_1(Yb_{20}–Er_2)/TiO_2$ located at 83.1 eV for Au $4f_{7/2}$ and 86.8 eV for Au $4f_{5/2}$, and for $Au_3–RE_1(Yb_{20}–Er_2)/TiO_2$ at 83.0 eV for Au $4f_{7/2}$ and 86.7 eV for Au $4f_{5/2}$, indicating the metallic phase of Au in the two samples (Fig. 3c).[25,26] The Y 3d spectra (Fig. 3d) show the doublet peaks of Y 3d of $Au_1–RE_1(Yb_{20}–Er_2)/TiO_2$ at 159.3 eV for Y $3d_{5/2}$ and 161.4 eV for Y $3d_{3/2}$, and for $Au_3–RE_1(Yb_{20}–Er_2)/TiO_2$ at 159.2 eV for Y $3d_{5/2}$ and 161.3 eV for Y $3d_{3/2}$, which can be attributed to the Y^{3+} ions.[27]

X-ray diffraction measurements (XRD) were carried out to detect the crystal structure of Au–RE/TiO_2 since the crystal phase influences the photo absorption and electron mobility significantly. For different Au loading (Fig. 4a), the diffraction peaks of Ti (PDF#05-0682), TiO_2 anatase (PDF#21-1272), and $NaYF_4$ (cubic phase, PDF#77-2402) can be observed for all samples. The diffraction peak of Au cannot be detected for $Au_1–RE_1(Yb_{20}–Er_2)/TiO_2$, which can be ascribed to the low loading of Au. However, it can be distinguished for $Au_3–RE_1(Yb_{20}–Er_2)/TiO_2$ as a face-centered cubic phase with a PDF number of 01-1172.

For different RE amounts (Fig. 4b), the characteristic peaks of Ti and anatase TiO_2 can be observed for all samples. The diffraction peak of $NaYF_4$ appears for $Au_1–RE_1(Yb_{20}–Er_2)/TiO_2$ and $Au_1–RE_3(Yb_{20}–Er_2)/TiO_2$, and the intensity increases with RE deposition time. For different concentrations of Yb^{3+} and Er^{3+} (Fig. 4c and d), the diffraction peak of $NaYF_4$ can be

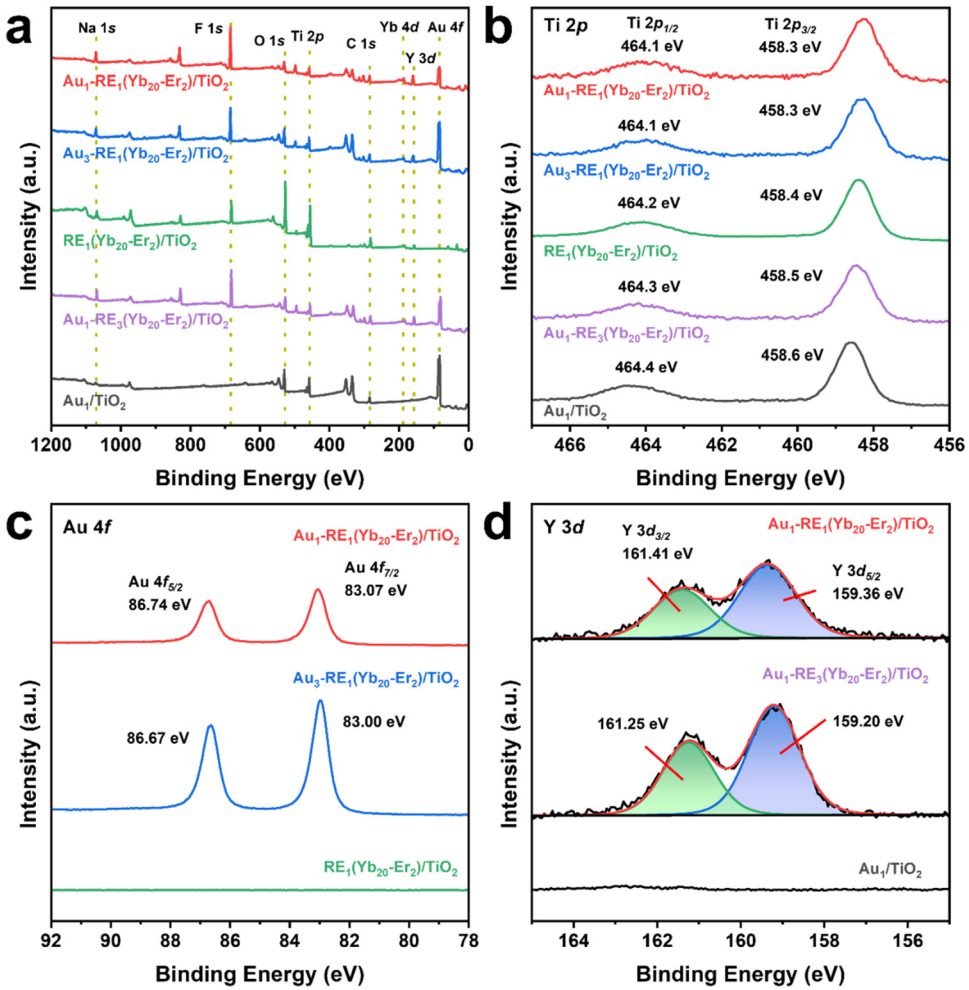

Fig. 3 XPS spectra of different samples. (a) Survey spectrum, (b) Ti 2p, (c) Au 4f of samples with different Au loading, and (d) Y3d of samples with different RE deposition amounts.

detected in Au_1–$RE_1(Yb_0$–$Er_2)/TiO_2$, Au_1–$RE_1(Yb_{20}$–$Er_0)/TiO_2$, and Au_1–$RE_1(Yb_{20}$–$Er_2)/TiO_2$. However, the peak of $NaYF_4$ cannot be observed in Au_1–$RE_1(Yb_{40}$–$Er_2)/TiO_2$) and Au_1–$RE_1(Yb_{20}$–$Er_4)/TiO_2$, which may be caused by excessive dopants of Yb^{3+} or Er^{3+} destroying the $NaYF_4$ lattice.[28]

3.4. Photothermal conversion ability

The photothermal conversion performance was evaluated in phosphate buffer saline (PBS) under NIR irradiation (Fig. 5a). After irradiation, the temperatures of TiO_2, Ti, and PBS increase to 46.7 °C, 44.4 °C, and 32.8 °C, respectively. The rise of temperature of TiO_2 is ascribed to the higher absorption and lower reflectance of TiO_2 NTAs than that of flat Ti.[29,30] The temperature of Au_1–$RE_1(Yb_{20}$–$Er_2)/TiO_2$ increases to 55.1 °C after irradiation, which is likely attributed to the photothermal oscillation of RE NPs, and possibly the LSPR effect of Au NPs.[31,32] In general, a photothermal temperature exceeding 70 °C has been found to be highly effective in eliminating bacteria. Meanwhile, at a relatively lower temperature from 50 to 60 °C, the bactericidal capability is somewhat reduced.[33] Moreover, the temperature of Au_1–$RE_1(Yb_{20}$–$Er_2)/TiO_2$ is lower than that reported in the literature. This further proves that it is less harmful to normal tissue cells, but still functional for killing bacteria.[34–36]

For $RE_1(Yb_{20}$–$Er_2)/TiO_2$ (Fig. 5b), a lack of Au NPs causes the temperature to increase to only 48.2 °C, which is not much higher that the temperature of TiO_2 after irradiation (46.7 °C), suggesting that Au NPs are necessary for the photothermal conversion. However, the temperature of Au_3–$RE_1(Yb_{20}$–$Er_2)/TiO_2$ increases to 51.9 °C, suggesting that the excessively high Au amount is not favorable for the photothermal conversion efficiency.

For samples with different RE deposition amounts (Fig. 5c), the temperature of Au_1–$RE_3(Yb_{20}$–$Er_2)/TiO_2$ reaches 55.5 °C, similar to that of Au_1–$RE_1(Yb_{20}$–$Er_2)/TiO_2$ (55.1 °C). This may be due to the saturation of absorption and conversion of NIR by RE NPs. For Au_1/TiO_2, without any RE decoration, the temperature increases to 49.8 °C after irradiation, indicating that Au NPs, in our case, are able to convert a certain amount of NIR into heat.

Furthermore, the increase of concentrations of Yb^{3+} from 20% to 40% (Fig. 5d) does not cause a significant change in the

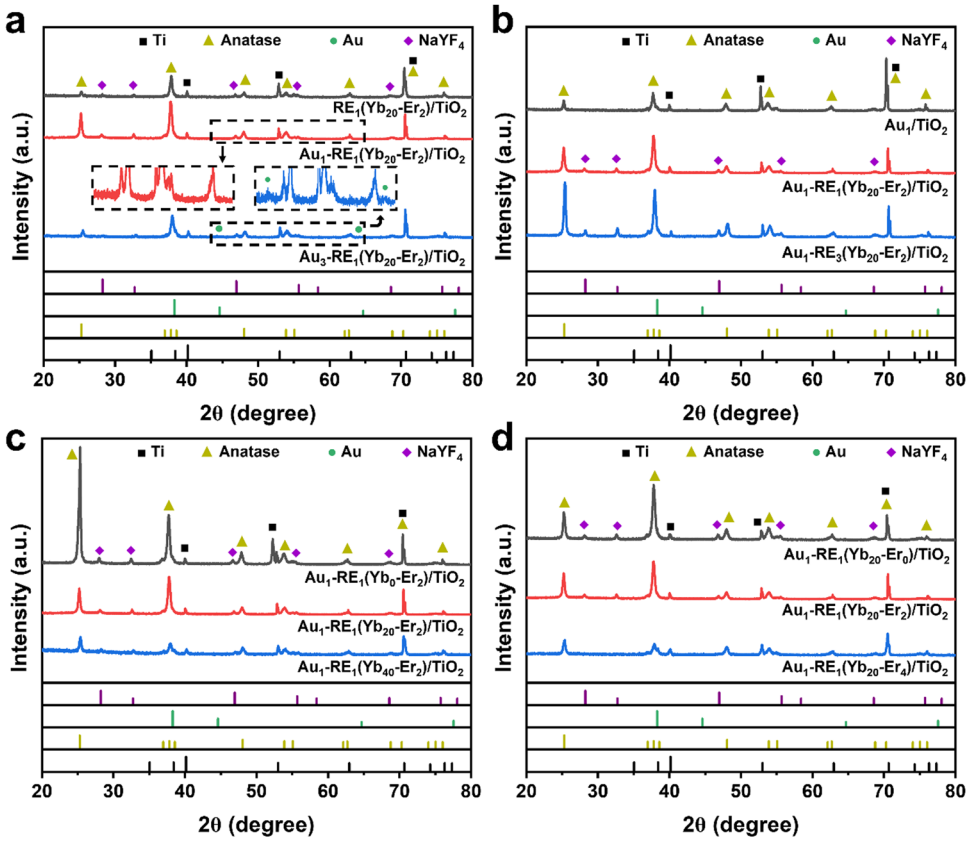

Fig. 4 XRD patterns of different samples. (a) Different Au loading, (b) different RE deposition amount, (c) different concentration of Yb^{3+}, and (d) different concentration of Er^{3+}.

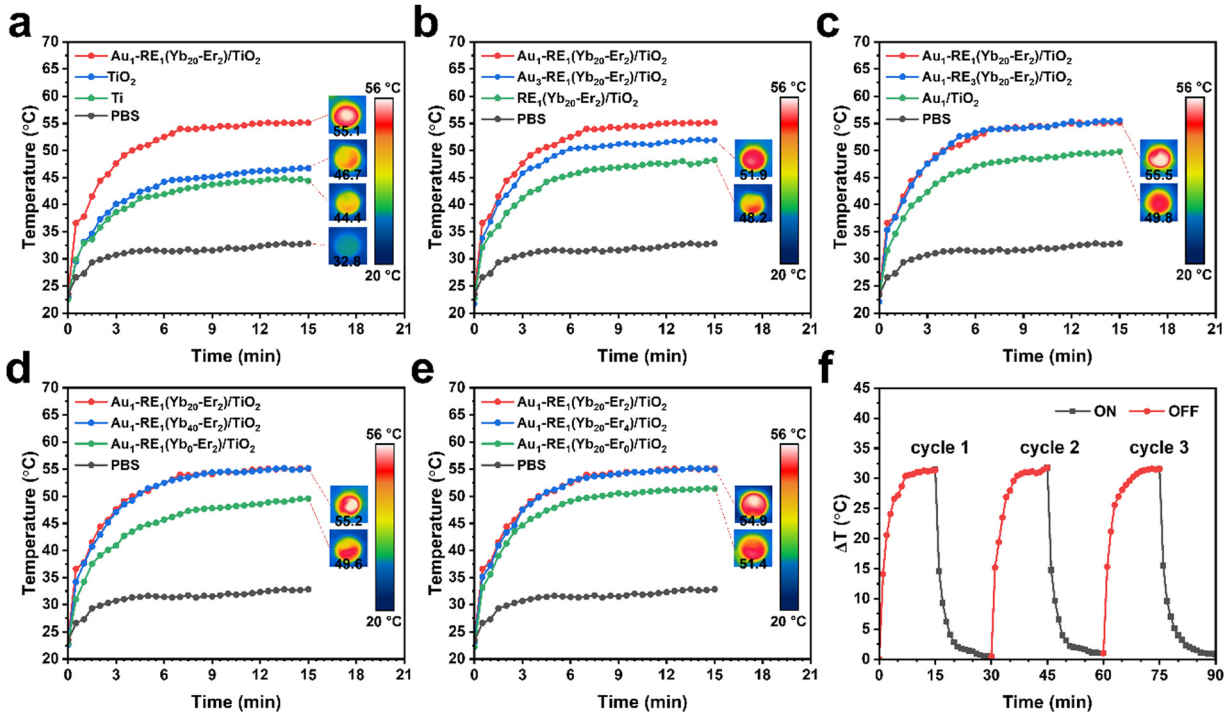

Fig. 5 Photothermal properties of samples under NIR irradiation. (a) Au_1–$RE_1(Yb_{20}$–$Er_2)/TiO_2$, TiO_2, Ti, and PBS, (b) different Au loading, (c) different RE deposition amount, (d) different concentration of Yb^{3+}, and (e) different concentration of Er^{3+}. (f) Photothermal stability of Au_1–$RE_1(Yb_{20}$–$Er_2)/TiO_2$ under NIR irradiation.

temperature rise of Au_1–$RE_1(Yb_{40}$–$Er_2)/TiO_2$ (55.2 °C). On the contrary, without Yb^{3+}, a temperature increase to 49.6 °C (Au_1–$RE_1(Yb_0$–$Er_2)/TiO_2$) is observed. This is similar to that of Au_1/TiO_2, owing to the lack of NIR absorption of RE NPs without Yb^{3+} as the light sensitizer. Similarly, increasing the concentrations of Er^{3+} from 2% to 4% (Fig. 5e) leads to a small change in the temperature of Au_1–$RE_1(Yb_{20}$–$Er_4)/TiO_2$ (54.9 °C). However, at a concentration of 0% Er^{3+}, Au_1–$RE_1(Yb_{20}$–$Er_0)/TiO_2$ shows a temperature of 51.4 °C after irradiation due to the absence of the activator Er^{3+}. The NIR can be absorbed, but not activated for upconversion.

To summarize, the factors that affect the photothermal conversion ability of the samples in order of importance are as follows: absorber Au, amount of RE NPs, concentration of sensitizers, and concentration of activators. Moreover, the photothermal conversion stability of Au_1–$RE_1(Yb_{20}$–$Er_2)/TiO_2$ is tested for three cycles of light exposure and off (Fig. 5f), suggesting that the photothermal ability can be retained in the cycles by transient light. The temperature increase and decrease rates, and the highest and lowest temperatures are similar to that of the first cycle.

3.5. ROS generation capability

The ROS generated by samples under NIR irradiation were detected through RhB degradation assays because ROS could degrade RhB and lead to a decrease in the UV-Vis spectra of solution. The RhB aqueous solution with Au_1–$RE_1(Yb_{20}$–$Er_2)/TiO_2$ shows the most significant reduction in intensity of absorbance, reaching a magnitude of 27% (Fig. 6 and Fig. S6, ESI†). Under NIR illumination, the luminescence of RE NPs is excited and visible light is emitted, which is absorbed by Au NPs to produce hot electrons to attack the adsorbed RhB molecules. Alternatively, the hot electrons can transfer to TiO_2 to produce electron–hole pairs that react with the solution to generate ROS.

The RhB removal percentage of $RE_1(Yb_{20}$–$Er_2)/TiO_2$ without Au NPs only reaches 11%, which is inferior to that of Au_1–$RE_1(Yb_{20}$–$Er_2)/TiO_2$ (Fig. 6a). The result suggests that the absence of Au leads to the lack of absorption of the visible light emitted by RE NPs, and thus produces less ROS. The removal percentage of RhB of Au_3–$RE_1(Yb_{20}$–$Er_2)/TiO_2$ decreases to 18% compared to that of Au_1–$RE_1(Yb_{20}$–$Er_2)/TiO_2$, suggesting that a high amount of Au is not beneficial for ROS generation. This can be attributed to the change in the morphology of Au leading to less absorption of the luminescence light emitted by RE NPs.

In the absence of RE NPs, it is observed that Au_1/TiO_2 exhibits a considerably low removal percentage of RhB (4%). This observation also suggests that Au NPs may possess the ability to absorb NIR, although it is extremely low (Fig. 6b). The removal percentage of RhB of Au_1–$RE_3(Yb_{20}$–$Er_2)/TiO_2$ (14%) is lower than that of Au_1–$RE_1(Yb_{20}$–$Er_2)/TiO_2$, which is possibly due to the excessive RE NPs on the surface of the sample. This affects the diffusion of ROS and the absorption of RhB on the

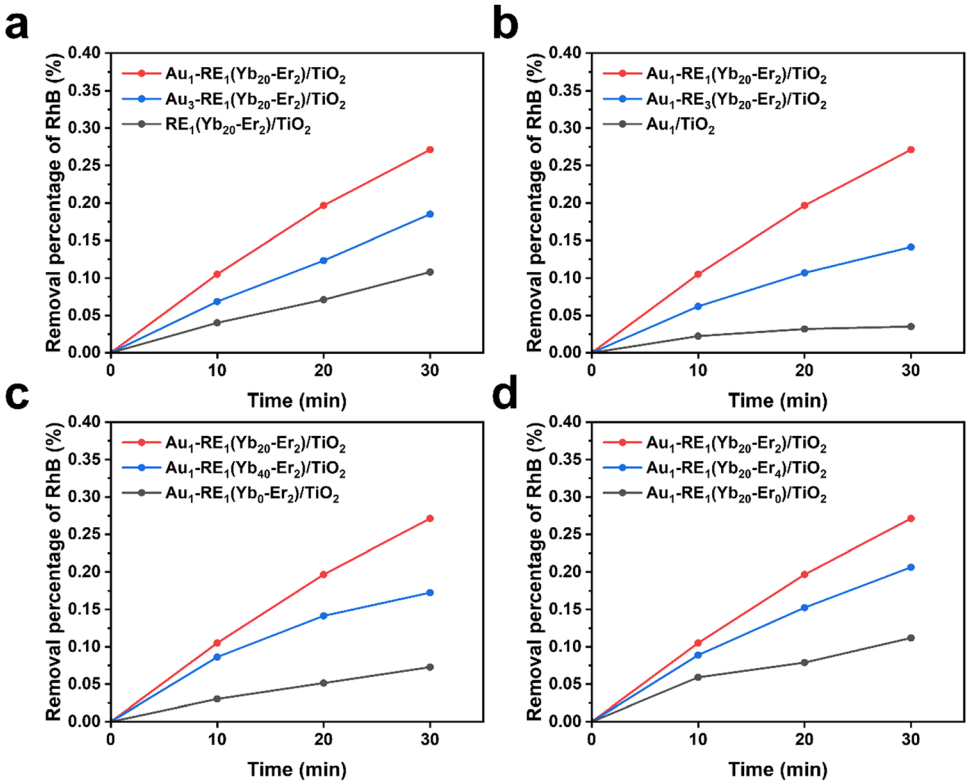

Fig. 6 The change of absorbance at 554 nm of rhodamine B at different irradiation times of NIR. (a) Different Au loading, (b) different RE deposition amount, (c) different concentration of Yb^{3+}, (d) different concentration of Er^{3+}.

TiO_2 nanotubes. The generation of ROS and degradation of RhB occur near or on the surface of the nanotubes.[37]

In addition, the concentration of sensitizer Yb and activator Er affects the ROS generation ability of the samples. Due to the absence of activator (Yb^{3+}), Au_1–$RE_1(Yb_0$–$Er_2)/TiO_2$ exhibits a low removal percentage of RhB of 7%. Compared to Au_1/TiO_2, the slightly higher ability for generating ROS can be attributed to the NIR absorption activity of Au NPs and Er^{3+} (Fig. 6c).[38] Increasing the concentration of Yb^{3+} to 40% in Au_1–$RE_1(Yb_{40}$–$Er_2)/TiO_2$ does not result in higher ROS generating ability (17%) compared to Au_1–$RE_1(Yb_{20}$–$Er_2)/TiO_2$. This is possibly attributed to the high concentration of Yb^{3+} leading to energy dissipation during long-distance transfer, and quenching by non-radiative relaxation in the lattice or surface defects.

Similarly, the absence of the activator (Er^{3+}) in Au_1–$RE_1(Yb_{20}$–$Er_0)/TiO_2$ suggests that the NIR absorbed by RE NPs cannot be converted into visible light, resulting in a low removal percentage of RhB of 11% (Fig. 6d). At high Er concentration, the removal percentage of RhB of Au_1–$RE_1(Yb_{20}$–$Er_4)/TiO_2$ is 21%, which is lower than that of Au_1–$RE_1(Yb_{20}$–$Er_2)/TiO_2$. This is attributed to energy dissipation by local cross relaxation in the upconversion luminescence process.

Overall, the presence or absence of Au, RE NPs, sensitizer Yb^{3+}, or activator Er^{3+}, has an impact on the generation of ROS. A lack of these factors leads to a significant reduction in ROS generation, and an excess of the absorber, sensitizer, or activator slightly decreases the ROS generation. Among these factors, the loading of RE NPs exhibits the most significant influence on the ROS generation ability. This is because the RE NPs directly affect the NIR absorption properties and surface morphology of the samples. In addition, the amount of ROS generated by Au_1–$RE_1(Yb_{20}$–$Er_2)/TiO_2$ is roughly estimated using the ROS produced by the Fenton reaction, which is about 2.4×10^{-6} mol ROS (Fig. S7, ESI†).

The type of ROS was evaluated using different ROS capture agents, for example, ABDA for $^1O_2$. ABDA can specifically capture $^1O_2$ by forming endoperoxide products, resulting in a decrease in the absorbance at characteristic bands of 342, 359, 378, and 400 nm. Fig. S8a (ESI†) shows the gradual decrease in the intensity of absorbance of the ABDA aqueous solution with Au_1–$RE_1(Yb_{20}$–$Er_2)/TiO_2$ under NIR irradiation, which confirms the generation of $^1O_2$. MV is used as the indicator of $^{\bullet}OH$. The reduction in the absorbance of the MV aqueous solution suggests the generation of $^{\bullet}OH$ by Au_1–$RE_1(Yb_{20}$–$Er_2)/TiO_2$ (Fig. S8b, ESI†). In addition, the $^{\bullet}O_2^-$ generation by Au_1–$RE_1(Yb_{20}$–$Er_2)/TiO_2$ is evaluated using NBT as an indicator. Reacting with $^{\bullet}O_2^-$, the color of NBT changes from a pale yellow to purple by the formation of insoluble formazan, which exhibits an absorbance at 530 nm. The increase in absorbance of the solution indicates the production of $^{\bullet}O_2^-$ by Au_1–$RE_1(Yb_{20}$–$Er_2)/TiO_2$ (Fig. S8c, ESI†).

3.6. Antibacterial property

The Gram-negative *E. coli* and Gram-positive *S. aureus* were used as model strains to simulate the biofilm contamination to evaluate the antibacterial property of Au_1–$RE_1(Yb_{20}$–$Er_2)/TiO_2$. First, *E. coli* was used to evaluate the biofilm removal of surfaces in different synthetic conditions under NIR irradiation (Fig. 7a and b). The control group was set using $RE_1(Yb_{20}$–$Er_2)/TiO_2$ in dark conditions (without NIR). $RE_1(Yb_{20}$–$Er_2)/TiO_2$ after NIR irradiation has extremely low antibacterial efficiency (1.8%). This is because the absence of Au NPs leads to the direct coupling of RE NPs with TiO_2, resulting in an extremely low upconversion efficiency and electron transport efficiency. According to the previous experiment, due to the absence of Au NPs, $RE_1(Yb_{20}$–$Er_2)/TiO_2$ has a photocurrent of 0.06 μA cm^{-2}, a temperature of 48.2 °C, and a RhB removal percentage of 11%. Such a low photoresponse performance has a slight damage to bacteria.

In the presence of Au NPs, Au_1–$RE_1(Yb_{20}$–$Er_2)/TiO_2$ exhibits a significantly higher antibacterial efficiency of 98.9% compared to $RE_1(Yb_{20}$–$Er_2)/TiO_2$, suggesting that Au_1–$RE_1(Yb_{20}$–$Er_2)/TiO_2$ with a photocurrent of 0.38 μA cm^{-2}, a temperature of 55.1 °C, and a RhB removal percentage of 27% can effectively eliminate the bacterial film.

The antibacterial efficiency of Au_3–$RE_1(Yb_{20}$–$Er_2)/TiO_2$ after NIR irradiation decreases to 47.6% with the photocurrent declining to 0.21 μA cm^{-2}, temperature declining to 51.9 °C, and RhB removal percentage declining to 18%, which is caused by the change in the amount and size of Au NPs. An increase in size and variations in the shape of Au NPs leads to a noticeable decrease in photocurrent, and a slight reduction in photothermal conversion ability and ROS generation. This is because of the poor alignment between the absorption of Au NPs and luminescence of RE NPs. Therefore, the change of Au NPs can influence the bactericidal efficiency by having a significant impact on the photocurrent of the sample.

After NIR irradiation, Au_1/TiO_2 has an antibacterial efficiency of 4.4%, which may be caused by the extremely low absorption efficiency of NIR of Au NPs. In addition, Au_1/TiO_2 shows a photocurrent of 0.05 μA cm^{-2}, a temperature of 49.8 °C, and a RhB removal percentage of 4%. Therefore, when compared to $RE_1(Yb_{20}$–$Er_2)/TiO_2$, the slightly higher antibacterial efficiency of Au_1/TiO_2 is attributed to its higher photothermal conversion ability.

When there is a high loading of RE NPs, the antibacterial efficiency is 24.4% for Au_1–$RE_3(Yb_{20}$–$Er_2)/TiO_2$ after NIR irradiation, and the photocurrent is 0.18 μA cm^{-2}, the temperature is 55.5 °C, the RhB removal percentage is 14%. Compared to Au_1/TiO_2, the presence of RE NPs results in an enhanced photoresponse performance and further increased antibacterial efficiency. Meanwhile, compared to Au_1–$RE_1(Yb_{20}$–$Er_2)/TiO_2$, excessive RE NPs cause a decrease in photocurrent and ROS generation.

In the absence of the sensitizer Yb^{3+}, Au_1–$RE_1(Yb_0$–$Er_2)/TiO_2$ exhibits an antibacterial efficiency of 26.2% after NIR irradiation, which is higher than that of Au_1/TiO_2 (4.4%). It may be attributed to the higher photocurrent observed in Au_1–$RE_1(Yb_0$–$Er_2)/TiO_2$. Although there are minimal variations in the temperature (49.6 °C for Au_1–$RE_1(Yb_0$–$Er_2)/TiO_2$ and 49.8 °C for Au_1/TiO_2) and ROS-mediated RhB removal

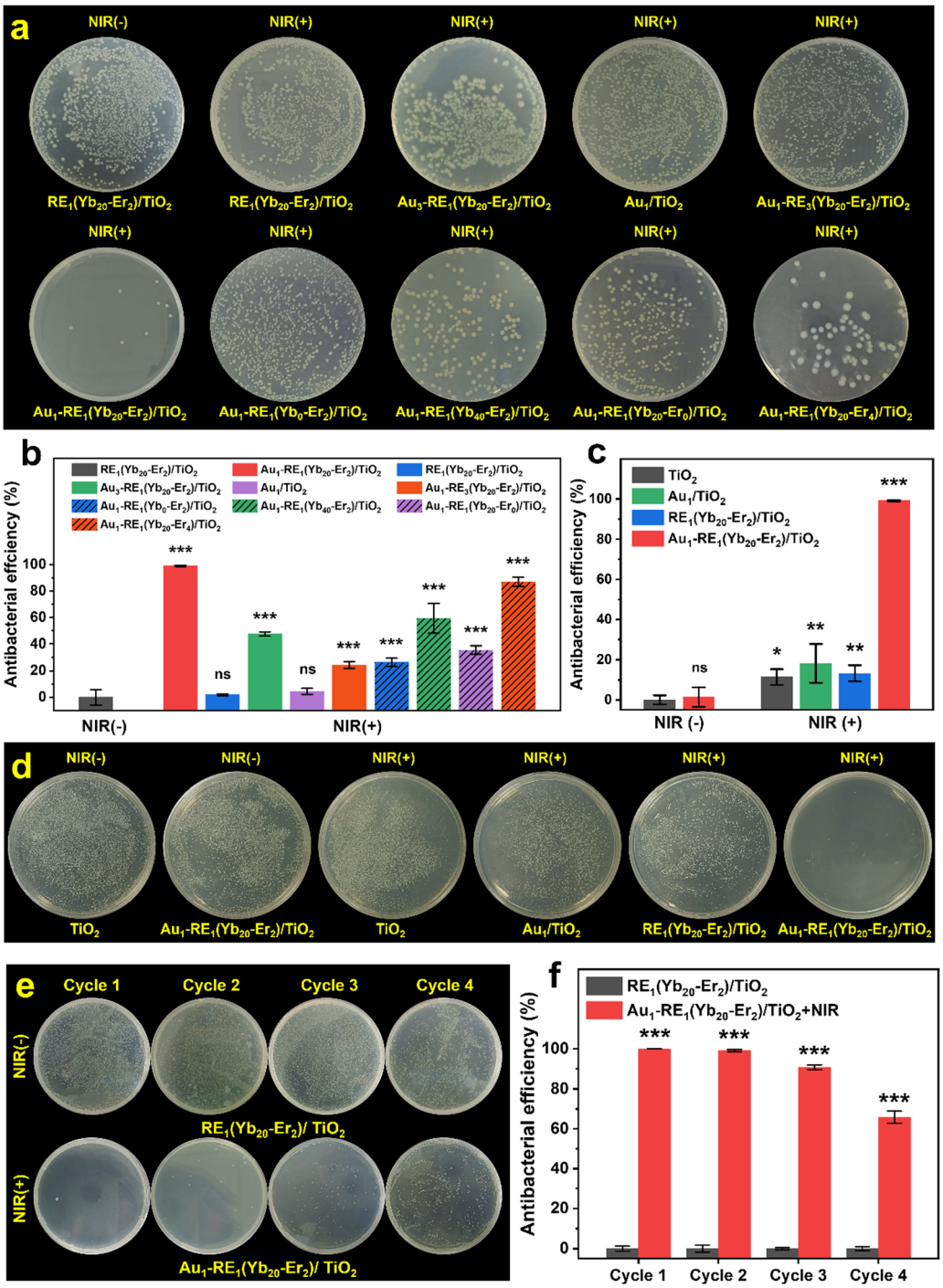

Fig. 7 Antibacterial property of samples. (a) Photographs of *E. coli* colonies after treatment with samples under NIR irradiation or without irradiation. (b) Antibacterial efficiency on the removal of the *E. coli* biofilm of samples. (c) and (d) Bacteria cyclic killing effects. The statistics were presented as means ± S. D., $n = 3$, *$p < 0.05$, **$p < 0.01$, ***$p < 0.001$, and ns (not significant).

percentages (7% for Au_1–$RE_1(Yb_0$–$Er_2)/TiO_2$ and 4% for Au_1/TiO_2), the significant difference in photocurrent suggests it is a key to the improvement of antibacterial efficiency of Au_1–$RE_1(Yb_0$–$Er_2)/TiO_2$ (0.18 μA cm^{-2} for Au_1–$RE_1(Yb_0$–$Er_2)/TiO_2$ and 0.05 μA cm^{-2} for Au_1/TiO_2).

However, when the deposition concentration of Yb^{3+} increases to 40%, the antibacterial efficiency decreases to 59.4%, which may be dominated by the photocurrent and ROS generation ability. The reason may be that an excessive amount of the sensitizer Yb^{3+} increases the useless energy dissipation in the luminescence process of RE NPs, which hinders the energy transfer from RE NPs to Au NPs. As a result, the photocurrent decreases from 0.38 μA cm^{-2} for Au_1–$RE_1(Yb_{20}$–$Er_2)/TiO_2$ to 0.13 μA cm^{-2} for Au_1–$RE_1(Yb_{40}$–$Er_2)/$

TiO_2. Similarly, the RhB removal percentages also decrease from 27% for Au_1–$RE_1(Yb_{20}$–$Er_2)/TiO_2$ to only 17% for Au_1–$RE_1(Yb_{40}$–$Er_2)/TiO_2$. Since the energy dissipation may produce heat through non-radiative relaxation, Au_1–$RE_1(Yb_{20}$–$Er_2)/TiO_2$ shows a similar photothermal conversion ability to Au_1–$RE_1(Yb_{20}$–$Er_2)/TiO_2$ (55.2 °C for Au_1–$RE_1(Yb_{20}$–$Er_2)/TiO_2$ and 55.1 °C for Au_1–$RE_1(Yb_{20}$–$Er_2)/TiO_2$ in temperature.

In the absence of an activator, the antibacterial efficiency of Au_1–$RE_1(Yb_{20}$–$Er_0)/TiO_2$ after NIR irradiation is 35.5%. Compared to Au_1/TiO_2, Au_1–$RE_1(Yb_{20}$–$Er_0)/TiO_2$ exhibits a higher photocurrent of 0.1 μA cm^{-2}, photothermal conversion ability of 51.4 °C, and removal percentage of RhB of 11%. However, the factors that lead to higher antibacterial efficiency of Au_1–$RE_1(Yb_{20}$–$Er_0)/TiO_2$ are photocurrent and temperature. This is because the ROS generation ability corresponding to 11% removal percentage of RhB is not enough to cause significant damage to bacteria (11% for RhB removal percentage for $RE_1(Yb_{20}$–$Er_2)/TiO_2$).

When the activator concentration is excessively high, it can have an impact on the antibacterial efficiency of Au_1–$RE_1(Yb_{20}$–$Er_4)/TiO_2$ after NIR irradiation. In this case, the antibacterial efficiency is 86.9%, which is slightly lower than that of Au_1–$RE_1(Yb_{20}$–$Er_2)/TiO_2$. In the previous experiment, Au_1–$RE_1(Yb_{20}$–$Er_4)/TiO_2$ exhibits a photothermal conversion ability comparable to that of Au_1–$RE_1(Yb_{20}$–$Er_2)/TiO_2$, with values of 54.9 °C and 55.1 °C for temperature, respectively. Additionally, Au_1–$RE_1(Yb_{20}$–$Er_4)/TiO_2$ demonstrates a slightly lower photocurrent and ROS generation ability compared to Au_1–$RE_1(Yb_{20}$–$Er_2)/TiO_2$, with values of 0.33 μA cm^{-2} and 0.38 μA cm^{-2} for current and 21% and 27% for RhB removal percentage, respectively. The effect of increasing the activator on the luminescence of RE NPs is not significant, which influences the photocurrent and ROS generation only to a small extent.

Overall, we have demonstrated that Au_1–$RE_1(Yb_{20}$–$Er_2)/TiO_2$ exhibits excellent antibacterial properties under our experimental conditions. The results show that Au loading dominates the generation of the photocurrent, the RE deposition amount affects both photocurrent and ROS generation, as well as the concentration of Yb^{3+}. The change on the concentration of Er^{3+} affects the photocurrent and photothermal conversion ability. Consequently, our findings suggest that the variation of the synthetic conditions impacts the generation of electrons most significantly, which leads to the antibacterial effect of samples. For example, for Au_1–$RE_1(Yb_{20}$–$Er_2)/TiO_2$, the role of the photoelectrons dominates the process of the removal of the biofilm; instead, the PDT and PTT slightly work.

Additionally, for Gram-positive bacteria, Au_1–$RE_1(Yb_{20}$–$Er_2)/TiO_2$ after NIR irradiation exhibits the lowest bacterial colonies of *S. aureus*, compared to other samples. The antibacterial efficiency reaches 99.1% compared to TiO_2 in the dark (Fig. 7c and d). The antibacterial results against *E. coli* and *S. aureus* show that Au_1–$RE_1(Yb_{20}$–$Er_2)/TiO_2$ have excellent antibacterial efficiency on biofilms under NIR irradiation.

We have further conducted antibacterial experiments over several cycles to explore the durability of the antibacterial efficiency of Au_1–$RE_1(Yb_{20}$–$Er_2)/TiO_2$ (Fig. 7e and f). In the first two cycles, Au_1–$RE_1(Yb_{20}$–$Er_2)/TiO_2$ shows antibacterial efficiencies of 99.9% and 99.1%, respectively, highlighting the reproducibility of the antibacterial properties of the surface. In the two subsequent cycles, the antibacterial efficiency gradually declines to 90.3% and 65.9% respectively. It can be thus concluded that Au_1–$RE_1(Yb_{20}$–$Er_2)/TiO_2$ can maintain an antibacterial efficiency for at least 3 cycles.

Taking the penetration depth in the tissue of NIR into consideration, the antibacterial properties of Au_1–$RE_1(Yb_{20}$–$Er_2)/TiO_2$ were assessed using a 3 mm thick pork. Fig. S9a (ESI†) shows the penetrated light intensity of NIR, which shows that the remaining power density is 29.0% for 694 mW cm^{-2}, 24.7% for 1326 mW cm^{-2}, and 24.8% for 1811 mW cm^{-2}. After penetration, the antibacterial efficiency of Au_1–$RE_1(Yb_{20}$–$Er_2)/TiO_2$ is measured to be 35.5% under 201 mW cm^{-2}, 49.4% under 327 mW cm^{-2}, and 74.9% under 449 mW cm^{-2} (Fig. S9b and c, ESI†). The results suggest that the antibacterial efficiency increases with the light intensity after penetration of the tissue, and highlight the potential application of Au_1–$RE_1(Yb_{20}$–$Er_2)/TiO_2$ in soft tissues.

The elimination of bacteria by photoresponsive antibacterial materials often involves the morphological change of bacteria, such as the damage of the bacterial cell membrane and the leakage of the internal substance.[39,40] Therefore, to further evaluate the antibacterial effect of Au_1–$RE_1(Yb_{20}$–$Er_2)/TiO_2$, we investigated the morphology of *E. coli*, the leakage of macromolecules, and the activity of dehydrogenase in the respiratory chain.

The morphology of *E. coli* on samples after NIR irradiation or under dark conditions is observed by scanning electron microscopy (Fig. 8a and Fig. S10a, ESI†). Significant deformation and rupture of the bacterial cell membrane are observed on the surface of Au_1–$RE_1(Yb_{20}$–$Er_2)/TiO_2$ after NIR irradiation, and the bacteria in other groups (Au_1–$RE_1(Yb_{20}$–$Er_2)/TiO_2$, TiO_2 + NIR, TiO_2) remained completely intact cellular structures, indicating that Au_1–$RE_1(Yb_{20}$–$Er_2)/TiO_2$ kills bacteria by damaging cell membranes under NIR exposure.

The leakage of macromolecules (protein and nucleic acid) of *E. coli* on samples is detected by measuring the absorbance of the bacterial suspensions after NIR irradiation (Fig. 8b and Fig. S10b, ESI†). Obviously, the release of nucleic acid and protein of Au_1–$RE_1(Yb_{20}$–$Er_2)/TiO_2$ after irradiation of NIR is significantly higher than that of Au_1–$RE_1(Yb_{20}$–$Er_2)/TiO_2$ under dark conditions, demonstrating that Au_1–$RE_1(Yb_{20}$–$Er_2)/TiO_2$ after irradiation of NIR for 15 min is sufficient to damage the cell membrane of *E. coli*, and cause the inside substances to leak out.

Respiratory chain dehydrogenase plays an essential role in the bacterial respiratory chain, which is involved in electron transfer during energy metabolism.[39] Iodonitrotetrazolium chloride (INT) can convert into dark-red iodonitrotetrazolium formazan when reduced by respiratory chain dehydrogenase and dissolved in organic solvents. However, if the respiratory chain activity is inhibited, the activity of respiratory chain dehydrogenase will be affected, showing a lighter apparent color. As shown in Fig. 8c and Fig. S10c (ESI†), the OD value

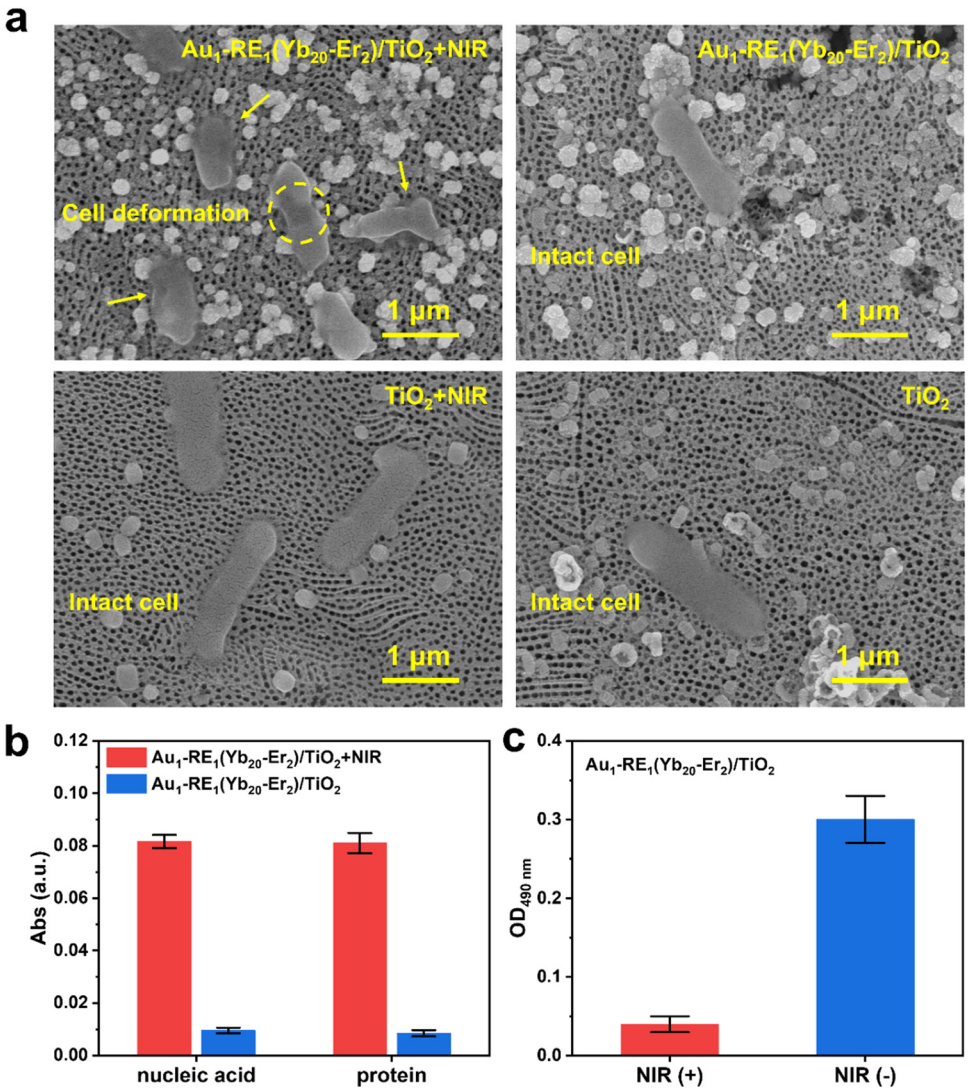

Fig. 8 Mechanism of bacterial death. (a) SEM images of *E. coli* of Au_1–$RE_1(Yb_{20}$–$Er_2)/TiO_2$ and TiO_2 under NIR irradiation or dark. (b) The release of nucleic acid and protein from *E. coli* of the Au_1–$RE_1(Yb_{20}$–$Er_2)/TiO_2$ group under NIR irradiation or dark conditions. (c) OD values at 490 nm of *E. coli* of Au_1–$RE_1(Yb_{20}$–$Er_2)/TiO_2$ mixed with INT solution under NIR irradiation or dark conditions.

of Au_1–$RE_1(Yb_{20}$–$Er_2)/TiO_2$ under NIR irradiation (Au_1–$RE_1(Yb_{20}$–$Er_2)/TiO_2$ + NIR, 0.04) is significantly lower than that of Au_1–$RE_1(Yb_{20}$–$Er_2)/TiO_2$ under dark conditions (Au_1–$RE_1(Yb_{20}$–$Er_2)/TiO_2$, 0.30), indicating that Au_1–$RE_1(Yb_{20}$–$Er_2)/TiO_2$ has an excellent impact on the respiratory chain of *E. coli* under the irradiation of NIR. The results thus demonstrate that Au_1–$RE_1(Yb_{20}$–$Er_2)/TiO_2$, after exposure to NIR, can eliminate *E. coli* by damaging the cell membranes, causing the release of proteins and nucleic acids, and inhibiting the activity of respiratory chain dehydrogenase.

3.7. EET mechanism

To explain the mechanism of photoelectrons on the elimination of bacteria, we further investigated the EET process between the bacteria and the materials by detecting the *I–V* curves of the materials inoculated with *E. coli*.[16,41] Under 980 nm NIR irradiation, Au_1–$RE_1(Yb_{20}$–$Er_2)/TiO_2$ inoculated with live *E. coli* shows the highest current (68 μA cm^{-2}), compared to Au_1–$RE_1(Yb_{20}$–$Er_2)/TiO_2$ inoculated with dead bacteria (45 μA cm^{-2}) and uninoculated bacteria (38 μA cm^{-2}), indicating that the activity of bacteria is necessary (Fig. 9a). However, the current difference between TiO_2 inoculated with live bacteria (40 μA cm^{-2}) and without inoculation (40 μA cm^{-2}) is negligible, suggesting that the highest current of Au_1–$RE_1(Yb_{20}$–$Er_2)/TiO_2$ results from the interaction between live bacteria and the sample; that is, EET between bacteria and materials under irradiation. Furthermore, the current difference of each group under dark condition is not significant (Fig. 9b), indicating that NIR illumination is crucial. In general, the EET process between bacteria and material can only occur during the contact between live *E. coli* and Au_1–$RE_1(Yb_{20}$–$Er_2)/TiO_2$, and NIR irradiation can generate photoelectrons.

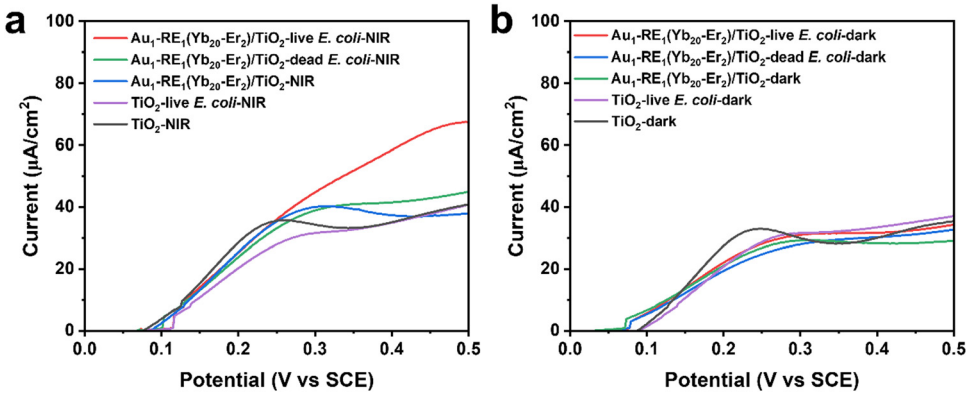

Fig. 9 I–V curves of TiO_2 and Au_1–$RE_1(Yb_{20}$–$Er_2)/TiO_2$ under (a) NIR irradiation or (b) dark condition.

3.8. Matching between absorption of Au NPs and luminescence of RE NPs

To understand the pathways of energy transfer, photoluminescence emission spectra were recorded for Au_1–$RE_1(Yb_{20}$–$Er_2)/TiO_2$ (Fig. 10a and b). RE NPs in $RE_1(Yb_{20}$–$Er_2)/TiO_2$ exhibits significant fluorescence emission peaks at 407 nm ($^2H_{9/2} \rightarrow {}^4I_{15/2}$, blue), 521 nm ($^2H_{11/2} \rightarrow {}^4I_{15/2}$, green), 541 nm ($^4S_{3/2} \rightarrow {}^4I_{15/2}$, green), and 653 nm ($^4F_{9/2} \rightarrow {}^4I_{15/2}$, red) under 980 nm NIR irradiation, with red emission (653 nm) being the predominant component, accounting for 90% in the peak area, of the overall luminous intensity. For Au_1–$RE_1(Yb_{20}$–$Er_2)/TiO_2$, these emission bands are significantly attenuated, indicating

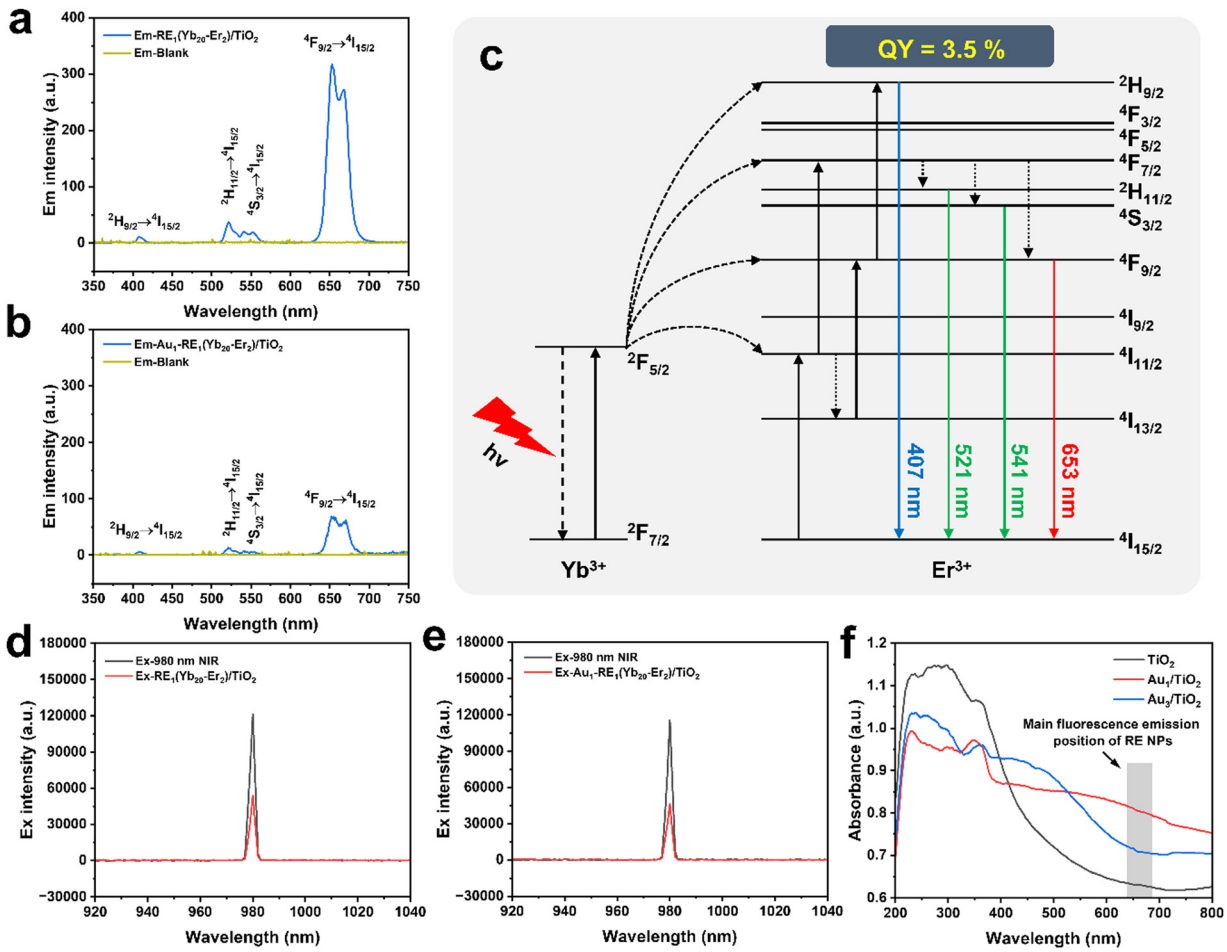

Fig. 10 Upconversion mechanism of RE NPs. (a) Emission spectra of $RE_1(Yb_{20}$–$Er_2)/TiO_2$ and blank. (b) Excitation spectra of $RE_1(Yb_{20}$–$Er_2)/TiO_2$ and blank. (c) Energy-level diagrams and upconversion energy transfer pathways in the Yb^{3+}–Er^{3+} pairs. (d) Emission spectra of Au_1–$RE_1(Yb_{20}$–$Er_2)/TiO_2$ and blank. (e) Excitation spectra of Au_1–$RE_1(Yb_{20}$–$Er_2)/TiO_2$ and blank. (f) UV-vis absorption spectrum of TiO_2, Au_1/TiO_2, and Au_3/TiO_2.

that the Au NPs in Au_1–$RE_1(Yb_{20}$–$Er_2)/TiO_2$ absorb emitted energy at these specific wavelengths. Moreover, by integrating the intensity of the emission spectra, it can be found that the light absorbed by Au NPs accounts for 93% of the total emission intensity of RE NPs. Fig. 10c shows the energy transfer pathways, where Yb^{3+}, as a sensitizer, absorbs 980 nm NIR and transfers to activator Er^{3+} and subsequently emits visible light as the excitons fall back to the ground states. Further, the quantum yield (QY) of RE NPs ($RE_1(Yb_{20}$–$Er_2)/TiO_2$) is measured to be 3.5% under 980 nm (2 W cm^{-2}) (Fig. 10a and d), which is higher than the values reported in the literature for similar upconversion materials.[42–44] Additionally, the QY of Au_1–$RE_1(Yb_{20}$–$Er_2)/TiO_2$ decreases to approximately 0.8%. This is possibly due to the absorption of emitted light by Au NPs (Fig. 10b and e).

The absorption spectrum of TiO_2, Au_1/TiO_2, and Au_3/TiO_2 was measured by UV-visible diffuse reflectance spectroscopy (DRS, Fig. 10f). The absorption band of TiO_2 is predominantly found in the UV region. With Au NPs, the absorption intensity in the UV region is slightly weakened due to the partial coverage by Au NPs. The absorption intensity in the visible region increases significantly, which can be ascribed to the LSPR of Au NPs. It is worth noting that samples with different Au loading exhibit different LSPR locations, which is approximately 600 nm for Au_1/TiO_2 and 500 nm for Au_3/TiO_2.[45] The main fluorescence emission peak of $RE_1(Yb_{20}$–$Er_2)/TiO_2$ is at 653 nm ($^4F_{9/2} \rightarrow {}^4I_{15/2}$), where the absorption of Au_1/TiO_2 absorbs more strongly than that of Au_3/TiO_2. The difference of the absorption range may be ascribed to the aggregation and sintering of Au at high amounts.

3.9. Biocompatibility of the surface

Considering the potential application of Au_1–$RE_1(Yb_{20}$–$Er_2)/TiO_2$ in the biological field, the biocompatibility of the samples becomes important. Improving the hydrophilicity of the material can promote cell adhesion and enhance the interaction of the material with cells and proteins. Therefore, the hydrophilicity of samples was measured by detecting the contact angles of different samples. Fig. 11a shows the contact angles of water on samples by varying the Au loading, RE deposition amount, and concentration of Yb^{3+} and Er^{3+}. The contact angles are 70.3° for Ti and 39.1° for TiO_2, respectively, which can be attributed to the unique nanotube structure present on the surface of TiO_2. The nanotube structure can provide a large surface area for water droplets to spread out and pores to infiltrate.[46] Additionally, the presence of surface hydroxyl

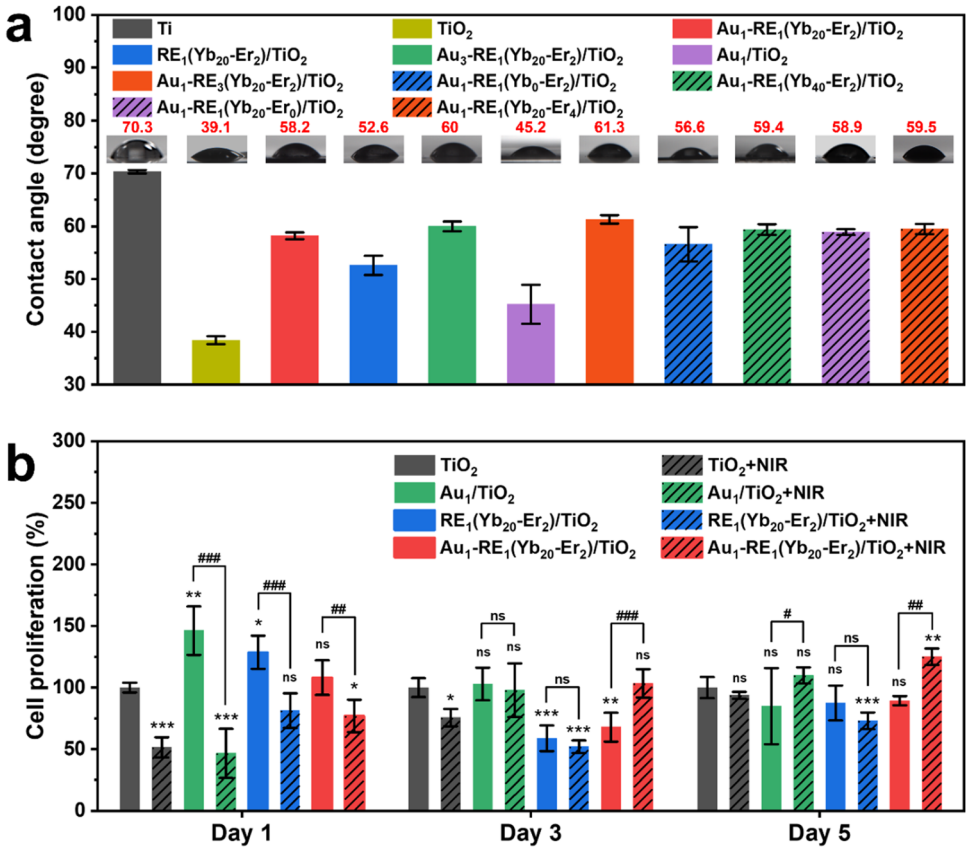

Fig. 11 (a) Contact angles on samples with different Au loading, RE deposition amount, and concentration of Yb^{3+} and Er^{3+}. (b) Cell proliferation of MC3T3-E1 cells on TiO_2, Au_1/TiO_2, $RE_1(Yb_{20}$–$Er_2)/TiO_2$ and Au_1–$RE_1(Yb_{20}$–$Er_2)/TiO_2$ for 1, 3, and 5 days. The statistics were presented as means ± S. D., $n = 3$, * $p < 0.05$, ** $p < 0.01$, *** $p < 0.001$ (compared with TiO_2 group), $^{\#}$ $p < 0.05$, $^{\#\#}$ $p < 0.01$, $^{\#\#\#}$ $p < 0.001$ (compared with the dark group), and ns (not significant).

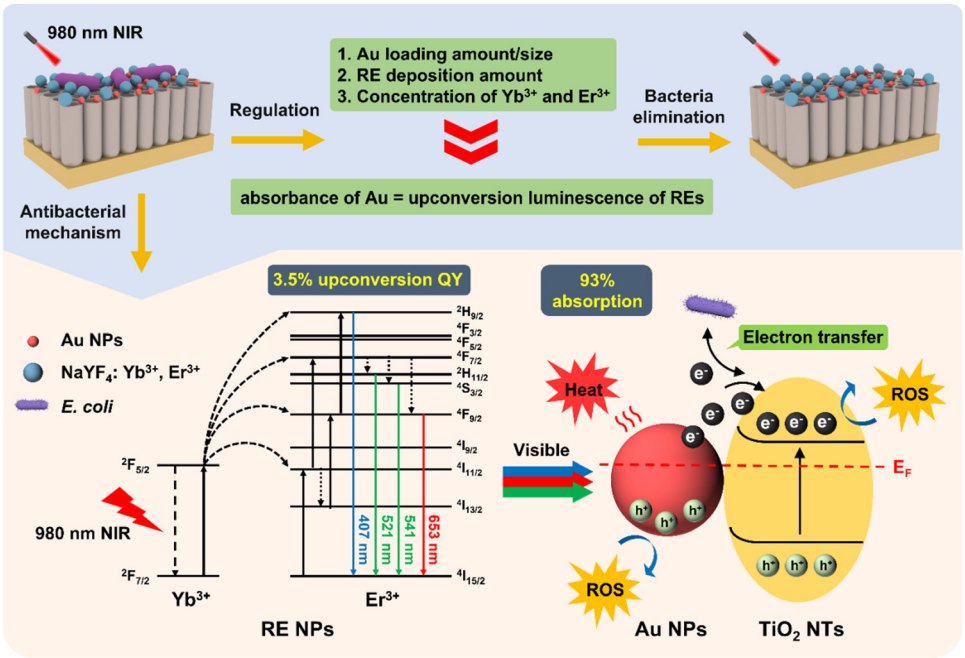

Fig. 12 Mechanism diagram of Au_1–$RE_1(Yb_{20}$–$Er_2)/TiO_2$ eliminating bacteria by regulating the absorption of Au NPs and upconversion of RE NPs.

groups further enhances the hydrophilicity of the TiO_2 surface, contributing to the reduced contact angle.[47] However, modifying samples with Au NPs and RE NPs result in contact angles (45.2° for Au_1/TiO_2, 52.6° for RE_1 $(Yb_{20}$–$Er_2)/TiO_2$, and 58.2° for Au_1–$RE_1(Yb_{20}$–$Er_2)/TiO_2$), and the contact angles increase slightly with the increase of the amount of Au NPs and RE NPs (60.0° for Au_3–$RE_1(Yb_{20}$–$Er_2)/TiO_2$ and 61.3° for Au_1–$RE_3(Yb_{20}$–$Er_2)/TiO_2$). For different concentrations of Yb^{3+} and Er^{3+}, the contact angles slightly change. These results suggest that Au NPs and RE NPs on the surface of the TiO_2 nanotubes improve the hydrophilicity of the material, and may promote the adhesion of cells, thereby improving the biocompatibility of the material.

To further estimate the biocompatibility of samples, CCK-8 assays were performed on different surfaces for 1, 3, and 5 days (Fig. 11b). Compared with TiO_2 under dark conditions, the cell proliferation rate of MC3T3-E1 at day 1 is higher when decorating Au NPs and RE NPs on TiO_2. After NIR treatment, the cell proliferation rates on TiO_2, Au_1/TiO_2, $RE_1(Yb_{20}$–$Er_2)/TiO_2$ and Au_1–$RE_1(Yb_{20}$–$Er_2)/TiO_2$ decrease somehow compared to the corresponding groups under dark conditions. At day 3, the cell proliferation rate of Au_1–$RE_1(Yb_{20}$–$Er_2)/TiO_2$ with NIR irradiation gradually recovers. Furthermore, at day 5, the cell proliferation rate of Au_1–$RE_1(Yb_{20}$–$Er_2)/TiO_2$ with NIR treatment is higher than that of TiO_2 with NIR treatment. The cell proliferation rate of Au_1–$RE_1(Yb_{20}$–$Er_2)/TiO_2$ under dark conditions is comparable to that of TiO_2 in the dark. These results indicate that the biocompatibility of Au_1–$RE_1(Yb_{20}$–$Er_2)/TiO_2$ is comparable to that of TiO_2, and it can be enhanced somehow by 980 nm NIR.

Considering that the metal ions may leak from the antibacterial surface, and may have an impact on cells or tissues, we detected the released ion (Au, Y, Yb, Er) concentrations from Au_1–$RE_1(Yb_{20}$–$Er_2)/TiO_2$ in SBF. Fig. S11 (ESI†) shows that after 14 days, the concentration of Au and Y ions released from Au_1–$RE_1(Yb_{20}$–$Er_2)/TiO_2$ are both less than 15 μg L^{-1}. The concentration of Yb and Er ions are not detected because the released concentrations are below the detection limit of the instrument (1 ppb). Such low ion concentrations hardly affect the cell behaviors.

3.10. Antibacterial mechanism

In conclusion, Au_1–$RE_1(Yb_{20}$–$Er_2)/TiO_2$ achieves a match between the absorption of Au NPs and the upconversion luminescence of RE by regulating the Au loading, RE deposition amount, and deposition concentration of Yb^{3+} and Er^{3+}, thus achieving an excellent antibacterial effect against the *E. coli* biofilm (Fig. 12). Noticeably, the activator (Yb^{3+}) in RE NPs absorbs 980 nm NIR light and transfers the energy to the sensitizer (Er^{3+}) for further conversion to visible light (Fig. 5). Then, the Au NPs on the TiO_2 nanotube arrays can absorb the visible light to produce hot electrons, thus producing heat and ROS. More importantly, once bacteria and Au_1–$RE_1(Yb_{20}$–$Er_2)/TiO_2$ contact, the flow of electrons outside the cell of bacteria can be obviously observed (Fig. 10). The current produced by the flow of electrons kill bacteria, cooperating with heat and ROS.

4. Conclusion

In this study, we have prepared an antibacterial surface on Ti and systematically investigated the parameters (activator, sensitizer, matrix, and absorber) that impact the upconversion

luminescence and photoelectron conversion efficiency, which eventually impact the ability to eliminate the biofilms with high durability. Compared to the photothermal conversion and ROS generation ability, the photocurrent is most significantly regulated. Thus, a new mechanism on the combating of bacteria has been provided, which may pave a way for innovative approaches to sterilization and disinfection, either directly on the surface or inside the tissue. Furthermore, the approaches on the fabrication of an antibacterial surface can be adapted to a wide range of other metal surfaces, including alloys, or magnesium.

Conflicts of interest

The authors declare no competing interests.

Acknowledgements

This work was financially supported by the National Natural Science Foundation of China (No. 22108179, X. Z., No. 82370996 and 82170997, L. X.), the Fundamental Research Funds for the Central Universities in China (No. YJ202081), and Project of Chengdu Science and Technology Bureau (No. 2022-YF05-00235-SN, X. Z.). The authors would like to thank Dr Yanping Huang from the Institute of Engineering Experimental Teaching Center, School of Chemical Engineering for SEM analysis, and Dr Yingming Zhu from New Energy and Low-Carbon Technology for the UV-vis adsorption measurement.

References

1 M. Geetha, A. K. Singh, R. Asokamani and A. K. Gogia, *Prog. Mater. Sci.*, 2009, **54**, 397–425.
2 L. Zhang, L. Chen and L. Wang, *Adv. Eng. Mater.*, 2020, **22**, 1901258.
3 S. Jafari, B. Mahyad, H. Hashemzadeh, S. Janfaza, T. Gholikhani and L. Tayebi, *Int. J. Nanomed.*, 2020, **15**, 3447–3470.
4 C. R. Arciola, D. Campoccia and L. Montanaro, *Nat. Rev. Microbiol.*, 2018, **16**, 397–409.
5 Y. Yang, S. Wang, L. Lu, Q. Zhang, P. Yu, Y. Fan and F. Zhang, *Angew. Chem., Int. Ed.*, 2020, **59**, 18380–18385.
6 N. Fomina, J. Sankaranarayanan and A. Almutairi, *Adv. Drug Delivery Rev.*, 2012, **64**, 1005–1020.
7 H. M. Yadav, J.-S. Kim and S. H. Pawar, *Korean J. Chem. Eng.*, 2016, **33**, 1989–1998.
8 Z. Zhou, B. Li, X. Liu, Z. Li, S. Zhu, Y. Liang, Z. Cui and S. Wu, *ACS Appl. Bio Mater.*, 2021, **4**, 3909–3936.
9 X. Bai, Y. Yang, W. Zheng, Y. Huang, F. Xu and Z. Bao, *Mater. Chem. Front.*, 2023, **7**, 355–380.
10 N. Diwanji and A. Bergmann, *Semin. Cell Dev. Biol.*, 2018, **80**, 74–82.
11 C. Zhang, X. Wang, J. Du, Z. Gu and Y. Zhao, *Adv. Sci.*, 2021, **8**, 2002797.
12 C. Chen, G. Chu, W. He, Y. Liu, K. Dai, J. Valdez, A. Moores, P. Huang, Z. Wang, J. Jin, M. Guan, W. Jiang, Y. Mai, D. Ma, Y. Wang and Y. Zhou, *Adv. Mater.*, 2023, **35**, e2207950.
13 X. Kang, F. Bu, W. Feng, F. Liu, X. Yang, H. Li, Y. Yu, G. Li, H. Xiao and X. Wang, *Adv. Mater.*, 2022, **34**, e2206765.
14 L. Tan, J. Li, X. Liu, Z. Cui, X. Yang, S. Zhu, Z. Li, X. Yuan, Y. Zheng, K. W. K. Yeung, H. Pan, X. Wang and S. Wu, *Adv. Mater.*, 2018, **30**, e1801808.
15 Z. Li, E. Wang, Y. Zhang, R. Luo, Y. Gai, H. Ouyang, Y. Deng, X. Zhou, Z. Li and H. Feng, *Nano Today*, 2023, **50**, 101826.
16 G. Wang, H. Feng, A. Gao, Q. Hao, W. Jin, X. Peng, W. Li, G. Wu and P. K. Chu, *ACS Appl. Mater. Interfaces*, 2016, **8**, 24509–24516.
17 M. Qi, M. Chi, X. Sun, X. Xie, M. D. Weir, T. W. Oates, Y. Zhou, L. Wang, Y. Bai and H. H. Xu, *Int. J. Nanomed.*, 2019, **14**, 6937–6956.
18 H. Lv, J. Liu, Y. Wang, X. Xia, Y. Li, W. Hou, F. Li, L. Guo and X. Li, *Front. Chem.*, 2022, **10**, 996264.
19 M. A. Khan and H. Idriss, *Wiley Interdiscip. Rev. Energy Environ.*, 2017, **6**, e254.
20 U. Ghosh, A. Pal and T. Pal, *Adv. Mater. Interfaces*, 2022, **9**, 2200465.
21 B. Chen and F. Wang, *Acc. Chem. Res.*, 2020, **53**, 358–367.
22 Y. Gao, J.-M. Lai and J. Zhang, *J. Semicond.*, 2023, **44**, 041901.
23 J. Zhao, J. Xu, X. Jian, J. Xu, Z. Gao and Y. Y. Song, *ACS Appl. Mater. Interfaces*, 2020, **12**, 23606–23616.
24 M. Altomare, N. T. Nguyen and P. Schmuki, *Chem. Sci.*, 2016, **7**, 6865–6886.
25 F. Wang, R. J. Wong, J. H. Ho, Y. Jiang and R. Amal, *ACS Appl. Mater. Interfaces*, 2017, **9**, 30575–30582.
26 A. Wang, S. Wu, J. Dong, R. Wang, J. Wang, J. Zhang, S. Zhong and S. Bai, *Chem. Eng. J.*, 2021, **404**, 127145.
27 K. Du, X. Xu, S. Yao, P. Lei, L. Dong, M. Zhang, J. Feng and H. Zhang, *CrystEngComm*, 2018, **20**, 1945–1953.
28 X. Chen, D. Peng, Q. Ju and F. Wang, *Chem. Soc. Rev.*, 2015, **44**, 1318–1330.
29 X. Zhang, G. Zhang, M. Chai, X. Yao, W. Chen and P. K. Chu, *Bioact. Mater.*, 2021, **6**, 12–25.
30 T. Csizmadia, M. Erdelyi, T. Smausz, T. Novak and B. Hopp, *J. Laser Micro. Nanoeng.*, 2015, **10**, 210–215.
31 Z. Tang, Q. Liu, J. Li, X. Wu, S. Zhan, G. Nie, J. Hu, S. Hu, Z. Xi, S. Wu, Y. Zhang, L. Shi and Y. Liu, *J. Lumin.*, 2019, **206**, 21–26.
32 J. Chen, Z. Ye, F. Yang and Y. Yin, *Small Sci.*, 2021, **1**, 2000055.
33 J. Sun, L. Song, Y. Fan, L. Tian, S. Luan, S. Niu, L. Ren, W. Ming and J. Zhao, *ACS Appl. Mater. Interfaces*, 2019, **11**, 26581–26589.
34 L. Zhang, C. Hu, M. Sun, X. Ding, H. B. Cheng, S. Duan and F. J. Xu, *Adv. Sci.*, 2023, **10**, e2300328.
35 K. Lv, G. Li, X. Pan, L. Liu, Z. Chen, Y. Zhang, H. Xu and D. Ma, *Adv. Healthcare Mater.*, 2023, **12**, e2300247.
36 X. Bao, L. Wu, Y. Yu, B. Xu, L. Cui, M. Zhou, Q. Wang and P. Wang, *Chem. Eng. J.*, 2023, **468**, 143584.
37 X. Zhou, N. Liu and P. Schmuki, *ACS Catal.*, 2017, **7**, 3210–3235.

38 Y. Yang, Z. Zhou, B. Mei, Y. Zhang and X. Liu, *Ceram. Int.*, 2021, **47**, 17139–17146.
39 X. Zhang, C. Yang and K. Yang, *ACS Appl. Mater. Interfaces*, 2020, **12**, 361–372.
40 X. Yin, J. Zhang, J. Xu, M. Tian, L. Li, L. Tan and Z. Li, *Compos. Sci. Technol.*, 2021, **202**, 108574.
41 G. Wang, H. Feng, L. Hu, W. Jin, Q. Hao, A. Gao, X. Peng, W. Li, K. Y. Wong, H. Wang, Z. Li and P. K. Chu, *Nat. Commun.*, 2018, **9**, 2055.
42 C. Homann, L. Krukewitt, F. Frenzel, B. Grauel, C. Wurth, U. Resch-Genger and M. Haase, *Angew. Chem., Int. Ed.*, 2018, **57**, 8765–8769.
43 J. C. Boyer and F. C. van Veggel, *Nanoscale*, 2010, **2**, 1417–1419.
44 I. N. Stanton, J. A. Ayres, J. T. Stecher, M. C. Fischer, D. Scharpf, J. D. Scheuch and M. J. Therien, *J. Phys. Chem. C*, 2017, **122**, 252–259.
45 M. Lickleder, R. Mohammadi, N. T. Nguyen, H. Park, S. Hejazi, M. Halik, N. Vogel, M. Altomare and P. Schmuki, *J. Phys. Chem. C*, 2019, **123**, 16934–16942.
46 J. Lin, W. Cai, Q. Peng, F. Meng and D. Zhang, *Scanning*, 2021, **2021**, 2717921.
47 Q. Li, E. Hu, K. Yu, R. Xie, F. Lu, B. Lu, R. Bao, F. Dai and G. Lan, *Adv. Fiber Mater.*, 2023, **5**, 1447–1466.